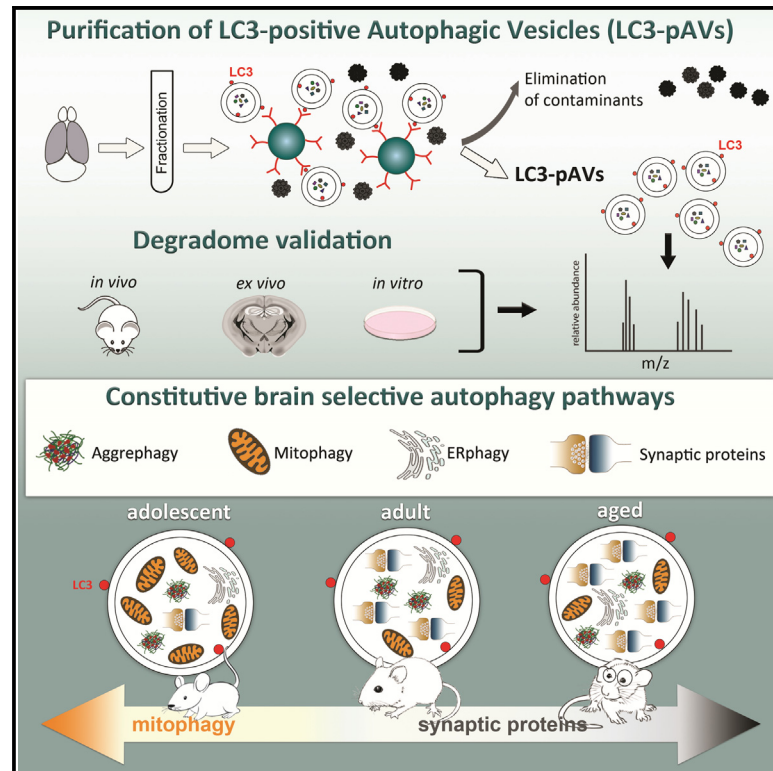


# Profiling of purified autophagic vesicle degradome in the maturing and aging brain

## Graphical abstract



## Authors

Emmanouela Kallergi,  
Devanarayanan Siva Sankar,  
Alessandro Matera, Angeliki Kolaxi,  
Rosa Chiara Paolicelli, Joern Dengjel,  
Vassiliki Nikolettou

## Correspondence

joern.dengjel@unifr.ch (J.D.),  
vassiliki.nikolettou@unil.ch (V.N.)

## In brief

Kallergi et al. provide a comprehensive map of the brain autophagic degradome. They reveal that protein aggregates, mitochondria, and endoplasmic reticulum, as well as synaptic proteins, are actively turned over by macroautophagy under basal conditions. These selective autophagy pathways are differentially regulated in the adolescent, adult, and aged brain.

## Highlights

- Proteomic profiling of intact LC3-positive autophagic vesicles of the forebrain
- Proteomic analysis of the forebrain autophagic degradome
- Identification of constitutive aggrephagy, mitophagy, and ER-phagy in the forebrain
- Enhanced mitophagy in young brain and sequestration of synaptic content in adult brain



## NeuroResource

# Profiling of purified autophagic vesicle degradome in the maturing and aging brain

Emmanouela Kallergi,<sup>1,4</sup> Devanarayanan Siva Sankar,<sup>2,4</sup> Alessandro Matera,<sup>3</sup> Angeliki Kolaxi,<sup>1</sup> Rosa Chiara Paolicelli,<sup>3</sup> Joern Dengjel,<sup>2,\*</sup> and Vassiliki Nikolettou<sup>1,5,\*</sup>

<sup>1</sup>Department of Fundamental Neurosciences, University of Lausanne, Lausanne, Switzerland

<sup>2</sup>Department of Biology, University of Fribourg, 1700 Fribourg, Switzerland

<sup>3</sup>Department of Biomedical Sciences, University of Lausanne, Lausanne, Switzerland

<sup>4</sup>These authors contributed equally

<sup>5</sup>Lead contact

\*Correspondence: joern.dengjel@unifr.ch (J.D.), vassiliki.nikolettou@unil.ch (V.N.)

<https://doi.org/10.1016/j.neuron.2023.05.011>

## SUMMARY

Autophagy disorders prominently affect the brain, entailing neurodevelopmental and neurodegenerative phenotypes in adolescence or aging, respectively. Synaptic and behavioral deficits are largely recapitulated in mouse models with ablation of autophagy genes in brain cells. Yet, the nature and temporal dynamics of brain autophagic substrates remain insufficiently characterized. Here, we immunopurified LC3-positive autophagic vesicles (LC3-pAVs) from the mouse brain and proteomically profiled their content. Moreover, we characterized the LC3-pAV content that accumulates after macroautophagy impairment, validating a brain autophagic degradome. We reveal selective pathways for aggrephagy, mitophagy, and ER-phagy via selective autophagy receptors, and the turnover of numerous synaptic substrates, under basal conditions. To gain insight into the temporal dynamics of autophagic protein turnover, we quantitatively compared adolescent, adult, and aged brains, revealing critical periods of enhanced mitophagy or degradation of synaptic substrates. Overall, this resource unbiasedly characterizes the contribution of autophagy to proteostasis in the maturing, adult, and aged brain.

## INTRODUCTION

Macroautophagy is a conserved degradation pathway with fundamental roles in cellular and organismal homeostasis. Previous work in cell lines and yeast demonstrated that a broad range of cytosolic constituents are sequestered by *de novo*-formed phagophores, which form mature double-membraned autophagic vesicles (AVs) and deliver their cargo to lysosomes for degradation.<sup>1</sup> A hallmark of the autophagic machinery is the conjugation of Atg8 family proteins to phosphatidylethanolamine on autophagic membranes.<sup>2</sup> Their primary role is in selective cargo sequestration and in the fusion of AVs with lysosomes by recruiting SNARE proteins, such as Syntaxin-17 (Stx17), onto the outer AV membrane.<sup>3</sup> Sequestration of organelles or aggregates requires selective autophagy receptors (SARs), which bridge the cargo with Atg8 on the phagophore membrane.<sup>4</sup>

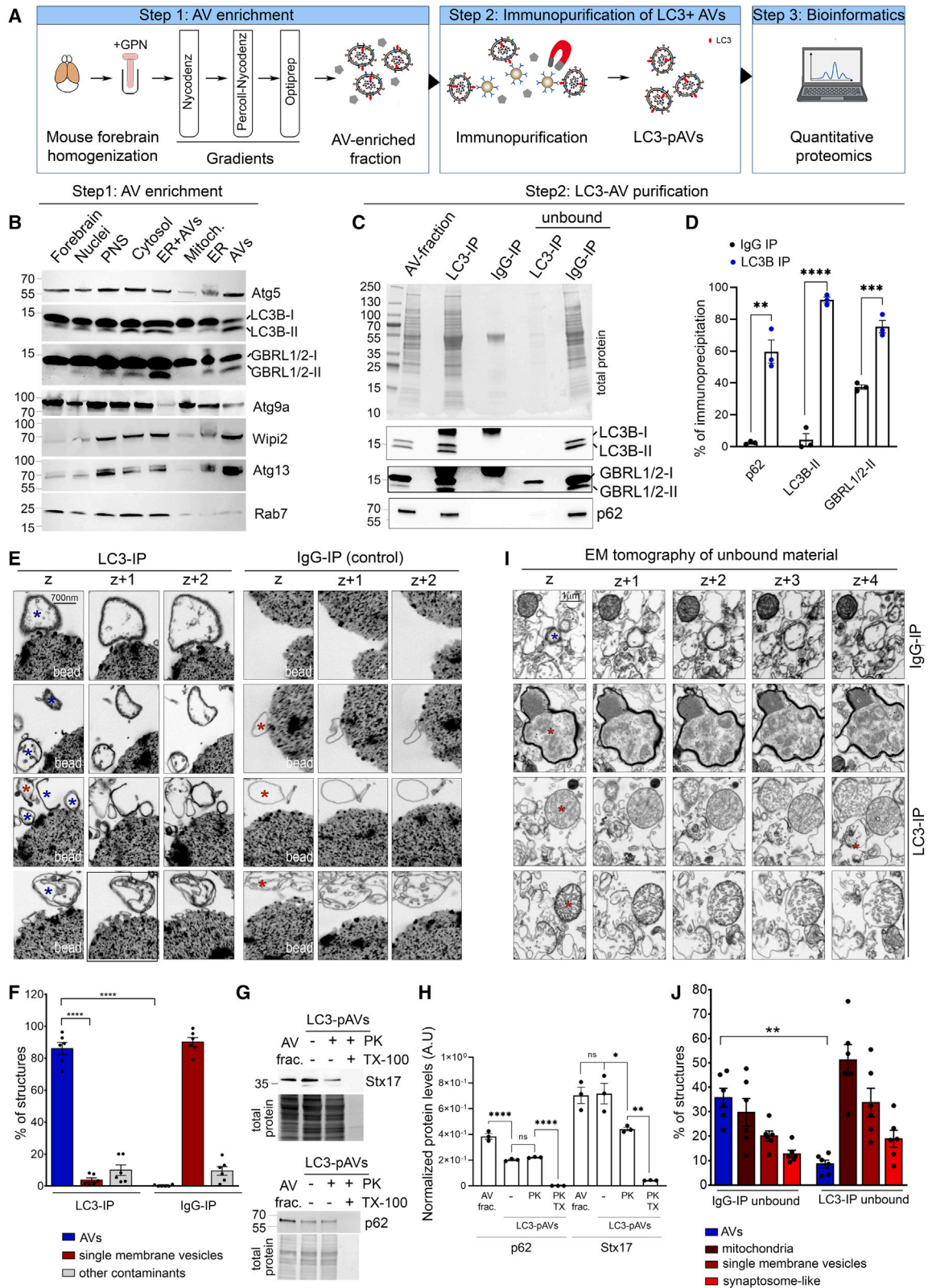
In humans, mutations in autophagy genes cause congenital diseases, including the Vici and beta-propeller protein-associated neurodegeneration (BPAN) syndromes, sharing prominent brain dysfunctions such as epilepsy, intellectual disability, and neurodegeneration.<sup>5</sup> Ablation of core-autophagy genes in neurons or glia also disrupts normal behavior, leading to motor deficits, memory impairment, altered sociability, and epilepsy.<sup>6–8</sup>

They are accompanied by deficits in synapse maturation, plasticity, and neurotransmitter release.<sup>9–16</sup>

Nevertheless, brain-selective autophagy pathways remain poorly characterized. Previous autophagic cargo analyses relied on targeting the expression of ascorbate peroxidase (APEX2) to AVs through fusion with hATG8s<sup>17–19</sup> or on enriching for AVs via cellular fractionation.<sup>20–22</sup> However, both approaches have significant drawbacks: APEX2 could be targeted to other cellular compartments, as Atg8 proteins have since been shown to also associate with non-autophagic endomembranes.<sup>23–27</sup> The AV-enrichment approach was recently used to profile the brain autophagic cargo<sup>28</sup>; however, its fidelity is compromised by the limited purity of the AV-enriched fraction.

To overcome these limitations, we developed a two-step protocol to purify LC3-positive AVs (LC3-pAVs) from the mouse forebrain. We analyzed their content by quantitative mass-spectrometry-based proteomics to identify autophagic substrates. We then validated a portion of these substrates as bona fide autophagic degradomes by demonstrating their accumulation upon brain autophagy deficiency or impaired autophagic flux. These analyses revealed the constitutive and selective degradation of aggregates, mitochondria, and the endoplasmic reticulum (ER), as well as many synaptic substrates. Finally, we compared





(legend on next page)

the autophagic degradome of the adolescent, adult, and aged brain to gain insight into the developmental and temporal dynamics of autophagic degradation.

## RESULTS

### Two-step purification of brain AVs

To purify brain AVs, we developed a two-step approach, combining cell fractionation and immunopurification. In the first step, mouse brains were homogenized and treated with glycyl-L-phenylalanine 2-naphthylamide (GPN) to eliminate acidic vesicles (Figure 1A). Homogenates were then subjected to consecutive gradients to obtain an AV-enriched fraction containing LC3, Gabarap1/2 and other autophagy proteins, but devoid of late endosomal markers such as Rab7 (Figure 1B), as previously described.<sup>12,15,28</sup> To ensure that this fraction contained intact AVs, we performed a proteinase K (PK) protection assay and found that p62/Sqstm1, a luminal aggrephagy receptor, was protected and only digested after permeabilization (Figures S1A and S1B). Moreover, PK-treatment decreased the levels of LC3 by half, consistent with its localization on both AV membranes (Figures S1A and S1B).

Ultrastructural examination of the PK-treated AV fraction confirmed not only the presence of intact AVs (mean = 38% of structures; Figures S1C and S1D) but also single-membraned vesicles, mitochondria, and synaptosome-like vesicles (Figures S1C and S1D). To eliminate these contaminants, whose content is also PK-insensitive, we introduced a second step, where AVs are immunopurified (Figures 1A, 1C, and 1D) using an antibody against LC3B that also recognizes LC3A (Figure S1E). As shown in Figures 1C and 1D, LC3 and p62 (Figure S1E), as well as Gabarap1 and 2 (Figures 1C and 1D), were all efficiently precipitated in the LC3-IP.

Recent work demonstrated that LC3 can be lipidated on endosomes, during LC3-associated phagocytosis (LAP) and LC3-associated endocytosis (LANDO).<sup>29</sup> Non-canonical LC3 lipidation requires several autophagic proteins, such as Beclin1, Vps34, Atg7, and Atg5, but occurs independently of ULK1 complex activity.<sup>30</sup> Therefore, we sought to exclude the possibility that the LC3-IP may enrich for single-membrane vesicles. To address this, we cultured neurons or astrocytes from transgenic mice, where LC3 is N-terminally fused with two

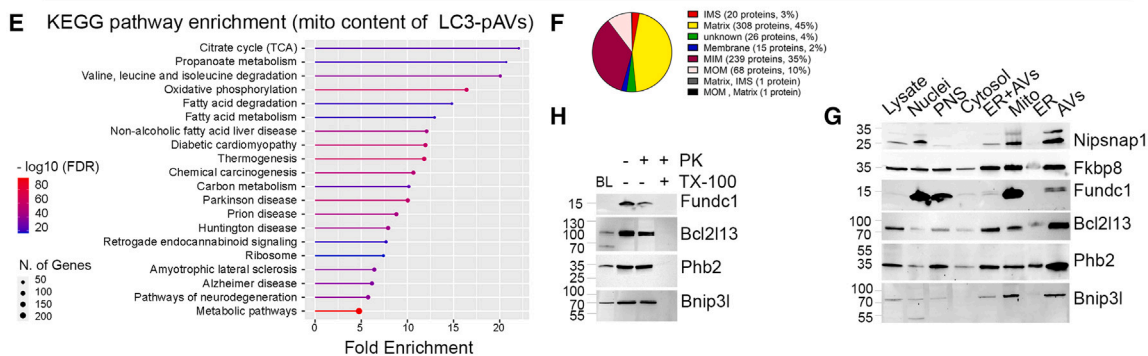
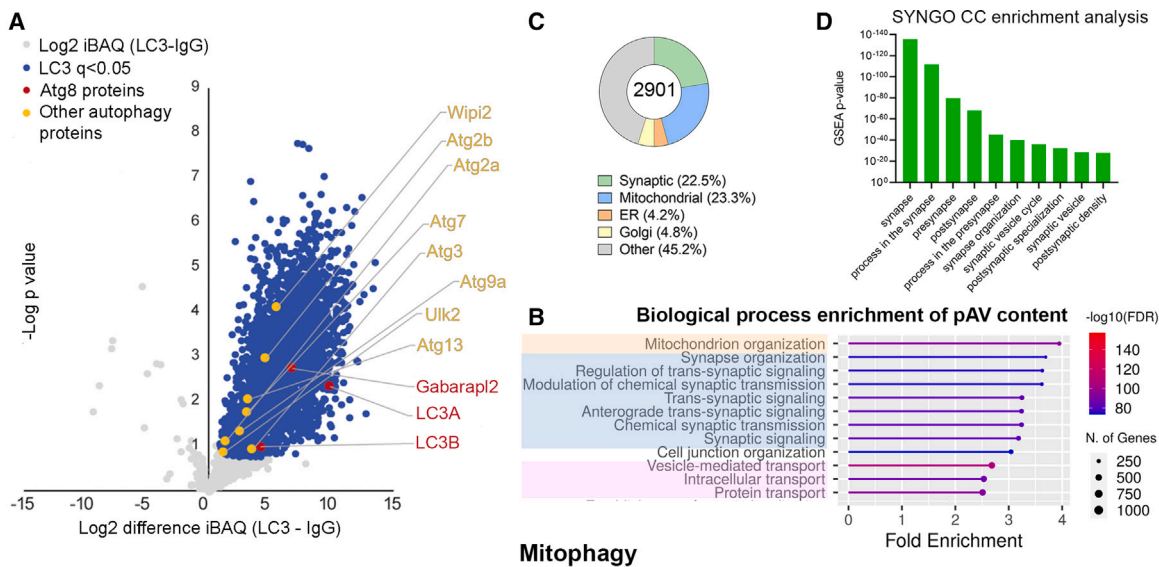
fluorophores, a pH-insensitive red fluorescent protein (RFP), and a pH-sensitive GFP (pCAG-RFP-GFP-LC3).<sup>31</sup> Yellow and red puncta represent neutral and acidified LC3-vesicles, respectively. Neurons (Figure S1F) and astrocytes (Figure S1G) exhibit yellow puncta (yellow arrowheads) and fluxed red puncta (white arrowheads). Three-h treatment with BafilomycinA1 (Baf), a lysosome acidification inhibitor, results in a perinuclear accumulation of large yellow puncta in both cell types (Figures S1F–S1I). We asked whether any yellow puncta remain after treating cells with an ULK1 kinase inhibitor (SBI-0206965) for 6 or 12 h, in the presence of Baf during the last 3 h. The 6-h treatment significantly reduced the number of LC3-puncta, while the 12-h treatment caused their complete absence both in neurons (Figures S1F and S1H) and astrocytes (Figures S1G and S1I). In addition, we treated forebrain cultures with Baf for 3 h, or with SBI-0206965 for 12 h in the absence or presence of Baf in the last 3 h. LC3-II failed to accumulate upon Baf-treatment in SBI-0206965-pretreated cultures (Figures S1J and S1K). p62 accumulated and the levels of Atg13 phosphorylated at S318 decreased upon SBI-0206965 treatment, consistent with ULK1 kinase inhibition (Figures S1J and S1K). Therefore, in neurons and astrocytes, LC3 lipidation is largely abolished by inhibition of AV biogenesis, suggesting that it primarily occurs on autophagic membranes.

To directly examine the AV enrichment (Figure 1A), we compared the LC3-IP and IgG-IP by electron tomography. As shown in Figure 1E, 87.8% of the LC3-IP structures represent double-membraned AVs (Figure 1E, blue asterisks; Figure 1F). The remaining material contained single-membraned vesicles (3.2% of total) or undefined membranes (9% of total) (Figure 1E, red asterisks; Figure 1F). However, these contaminants were found to a greater extent in the IgG-IP (Figure 1E, red asterisks; Figure 1F) making it a necessary control for further experiments. As a proxy of the ability of LC3-pAVs to fuse with lysosomes, we found that Stx17, a SNARE facilitating AV-lysosomal fusion,<sup>3</sup> was present in LC3-pAVs and was PK sensitive (Figures 1G and 1H), indicating its localization on the AV outer membrane. By contrast, p62 was protected from PK and only digested upon permeabilization, consistent with its localization in the AV lumen (Figures 1G and 1H).

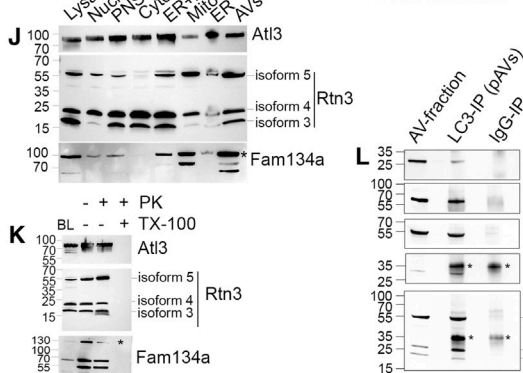
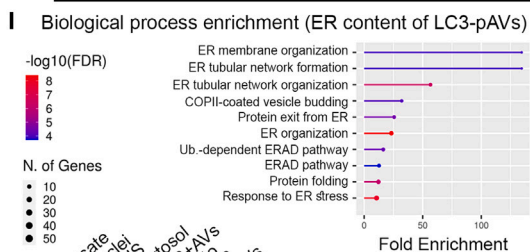
We also examined whether some AVs escape the LC3-IP by comparing the unbound material of LC3- and IgG-IPs by electron tomography. The IgG-IP unbound material resembled the

### Figure 1. Two-step purification of brain LC3-positive autophagic vesicles (LC3-pAVs)

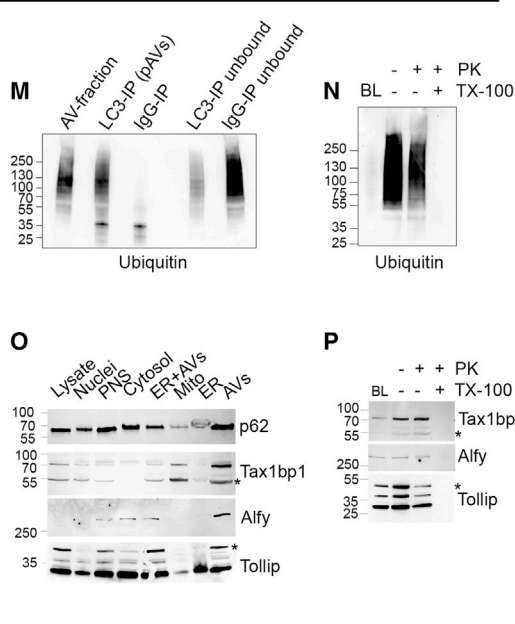
- (A) Schematic of the two-step protocol.  
 (B) Western blot of the fractions from Step1 with the indicated antibodies.  
 (C) Western blot with the indicated antibodies of LC3-IP, IgG-IP, and their respective unbound materials.  
 (D) Graph shows the enrichment of p62, LC3, and GBRL1/2 in the LC3-IP and IgG-IP from the total input, calculated as:  $\frac{\text{densitometric intensity of eluted}}{2.5 \times \text{densitometric intensity of Av fraction}} \times 100\%$ . n = 3, statistical analyses by unpaired t test. p62: p < 0.0014; LC3-II: p < 0.0001; Gabarap1/2-II: p = 0.0008.  
 (E) Representative electron micrographs of LC3-IP and IgG-IP material. AVs, blue asterisks; contaminants, red asterisks.  
 (F) Graph shows the percentage of the different structures in the LC3-IP and IgG-IP. n = 6, statistical analyses by one-way ANOVA (Tukey's multiple comparison test, F(5, 30) = 313.2).  $P_{\text{LC3-IP-IgG-IP}} < 0.0001$ ,  $P_{\text{LC3-IP-AVs-LC3-IP-single-membrane vesicles}} < 0.0001$ . Scale bar, 700 nm.  
 (G) Western blot of the PK-treated LC3-pAVs in the presence or absence of Triton X-100, using the indicated antibodies.  
 (H) Graph shows the normalized protein levels of p62 and Stx17. n = 3, statistical analyses by one-way ANOVA. p62: F(3,8) = 196.2, p < 0.0001 (Tukey's multiple comparison test  $P_{\text{AV frac. -PK}} < 0.0001$ ,  $P_{\text{-PK+PK}} = 0.6304$ ,  $P_{\text{+PK+PK+TX}} < 0.0001$ ). Stx17: F(3,8) = 37.59, p < 0.0001 (Tukey's multiple comparison test  $P_{\text{AV frac. -PK}} = 0.9975$ ,  $P_{\text{-PK+PK}} = 0.0221$ , and  $P_{\text{+PK+PK+TX}} = 0.0026$ ).  
 (I) Representative electron micrographs of the unbound material of the IgG-IP or LC3-IP. AVs, blue asterisks; contaminants, red asterisks.  
 (J) Graph shows the percentage of the different structures in the IgG-IP or LC3-IP unbound material. n = 6, statistical analyses by one-way ANOVA (Tukey's multiple comparison test, F(7, 40) = 10.93). AVs:  $P_{\text{LC3-unbound-IgG-unbound}} = 0.0014$ . Scale bar, 1  $\mu\text{m}$ .  
 (D, F, H, and J) Bars represent mean values  $\pm$  SEM.



**ER-phagy**



**Aggrephagy**



(legend on next page)

AV-enriched fraction, containing 35.7% of AVs (Figure 1I, AV denoted by blue asterisk; Figure 1J). The LC3-IP unbound material was poor in AVs (8.5%) but contained various non-autophagic structures, including axons (Figure 1I), mitochondria (51.2%), single-membrane vesicles (33.7%), and synaptosome-like vesicles (18.8%) (Figure 1I, red asterisks; Figure 1J). Therefore, the two-step procedure greatly enriches for AVs while excluding the majority of contaminating structures.

### Brain LC3-pAVs comprise synaptic and selective autophagy content

LC3-pAVs and IgG controls were profiled by quantitative proteomic analyses. We identified 2,901 proteins that were significantly enriched in the LC3-IP, compared with the IgG-IP (Figure 2A, blue circles t test,  $q < 0.05$ ,  $n = 3$  biological replicates each), and were recognized by at least one unique peptide (FDR  $< 0.01$ ). We coin this the LC3-pAV content (Table S1). This content includes LC3B as well as LC3A and Gabarapl2, consistent with LC3 antibody recognizing LC3A (Figures S1E and 1C). Several core-autophagy proteins, including Ulk2, Wipi2, Atg7, Atg2a, Atg13, and Atg9 were also present (Figure 2A).

Notably, 62% of the brain LC3-pAV content (1,812 proteins) was common with that of cell lines<sup>21</sup> (Figure S2A; Table S2), representing housekeeping functions (Figure S2B). The remaining 38% was brain-specific, displaying similar abundance with the common content (Figure S2C). We then compared the LC3-pAV content with the proteins detected in the PK-treated AV-enriched fraction.<sup>28</sup> We found that the 26% of proteins that were absent from that previous analysis (Figure S2A; Table S3) were enriched for roles in mitophagy (Figure S2D).

The forebrain contains mainly excitatory neurons, followed by inhibitory neurons and glia. Consistently, LC3-pAV content proteins are expressed in different cell types (Figure S2E),<sup>32</sup> with 15.5% unique in excitatory neurons, 14.3% in inhibitory neurons, 6.9% in astrocytes, 8.7% in oligodendrocytes, and 2.6% in microglia. The remaining 48.1% are proteins expressed in more than one brain cell type (Figure S2E).

Biological process analysis of the LC3-pAV content showed enrichment for mitochondrial organization, synaptic organization, synaptic signaling, and protein transport (Figure 2B). Consistently, comparisons with the SYNGO, Mitocarta 3.0, and ER-Golgi proteomes (Human Protein Atlas) indicated that it is composed of 654 synaptic (22.5%), 678 mitochondrial (23.3%), 122 ER (4.2%), and 140 Golgi proteins (4.8%) (Figure 2C; Table S4). The synaptic content showed widespread localization across pre- and postsynaptic compartments (Figure 2D), and roles in the synaptic vesicle cycle, modulation of synaptic transmission and trans-synaptic signaling (Figure S2F). Moreover, synaptic proteins featured among the most abundant proteins of the LC3-pAV content (abundance  $> 8$ -fold enrichment and  $p < 0.001$ ) (Figures S2G and S2H). Therefore, these functionally diverse and widely distributed synaptic proteins represent the abundant synaptic cargo of macroautophagy.

Kyoto Encyclopedia of Genes and Genomes (KEGG) pathway analysis indicated that LC3-pAV mitochondrial proteins are involved in the trichloroacetic acid (TCA) cycle, amino acid degradation, and fatty acid metabolism (Figure 2E). Cellular component analysis against the Mitocarta 3.0 database<sup>33</sup> indicated that most are localized in the matrix, followed by those in the mitochondrial inner and outer membranes (Figure 2F). The presence of mitochondrial proteins with diverse functions and localizations invites the speculation that brain mitophagy may occur constitutively under basal conditions. Consistently, the LC3-pAV content also includes six mitophagy receptors (Nipsnap1, Fkbp8, Fundc1, Bnip3l, Phb2, and Bcl2l13), which were confirmed in the AV fraction (Figure 2G) and PK-protected in LC3-pAVs (Figure 2H).

Comparison of the LC3-pAV content with the ER-protein atlas<sup>34</sup> revealed that of the 524 ER-resident proteins, 122 proteins (4.2% of AV content), are present in LC3-pAVs (Figure 2C; Table S4). Biological process analysis indicated functions in ER formation and organization, COPII-vesicle budding, and the ER-associated protein degradation (ERAD) pathway (Figure 2I). We also found three ER-phagy receptors (Calcoco1, At13, and

### Figure 2. Proteomic profiling of brain LC3-pAV content

- (A) Volcano plot of enriched proteins (t test,  $q < 0.05$ ) in LC3-IP compared with IgG-IP ( $n = 3$ ). iBAQ protein abundances were  $\log_2$  transformed and normalized to the median of the respective experiment.
- (B) Biological process enrichment analysis of the adult LC3-pAV content. Size and color of the bubble represent number of genes and enrichment significance, respectively.
- (C) Percentages of synaptic, mitochondrial, ER, and Golgi proteins of the adult LC3-pAV content.
- (D) Subcellular localization of the synaptic LC3-pAV content based on the Syngo database with their corresponding GSEA p values.
- (E) KEGG pathway enrichment analysis of the mitochondrial LC3-pAV content. Size and color of bubbles represent number of genes and enrichment significance, respectively.
- (F) Submitochondrial localization of the mitochondrial LC3-pAV content.
- (G) Western blot of fractions of Step1 using the indicated antibodies.
- (H) Western blot of PK-treated LC3-pAVs using the indicated antibodies.
- (I) Biological process enrichment analysis of the ER LC3-pAV content. Size and color of bubbles represent number of genes and enrichment significance, respectively.
- (J) Western blot of fractions of Step1 using the indicated antibodies.
- (K) Western blot of PK-treated LC3-pAVs using the indicated antibodies.
- (L) Western blot of LC3-pAVs using the indicated antibodies.
- (M) Western blot of LC3-pAVs for ubiquitin.
- (N) Western blot of PK-treated LC3-pAVs for ubiquitin.
- (O) Western blot of fractions of Step1 using the indicated antibodies.
- (P) Western blot of PK-treated LC3-pAVs using the indicated antibodies.
- (J–L and O–P) Asterisks, non-specific bands.



Rtn3), two of which were confirmed in the AV fraction (Figure 2J) and PK-protected in LC3-pAVs (Figure 2K). We also found FAM134a, previously proposed as an ER-phagy receptor under stress<sup>35</sup> (Figures 2J and 2K). These results suggest that ER-phagy may occur constitutively in brain cells, consistent with recent work demonstrating the autophagic degradation of ER proteins in the presynaptic compartment of cultured neurons.<sup>14</sup> Of the thirteen ER proteins (Atla1, Sac1, D3z7g3, Rtn4, Calx, Calr, Calu, Tecr, Ar6p1, Rtn3, Rtn1, Vapa, and Vamp7) suggested as autophagic substrates in the Kujipers et al. study,<sup>14</sup> seven (Sac1/Sacm1l, Calr, Calu, Tecr, Rtn3, Vapa, and Vamp7) were included in the LC3-pAV content (Table S4), and some were biochemically validated in LC3-pAVs (Figure 2L).

Consistent with identifying K48 and K63-ubiquitin crosslinks by mass spectrometry, LC3-pAVs contained (poly)-ubiquitinated proteins (Figure 2M), which are mostly PK-protected (Figure 2N). They also contained three aggrephagy receptors (Alfy/Wdfy3, Tax1bp1, and Tollip), which were confirmed and PK-protected in LC3-pAVs (Figures 2O and 2P). In addition, p62, already biochemically validated in the lumen of LC3-pAVs (Figures 1G and 1H), was identified in LC3-pAVs and not in the IgG control. This was also the case upon western blotting of the AV-enriched fraction; however, due to the limited number of datapoints, we were unable to quantify the enrichment by MS (Figure 2O).

These findings suggest constitutive aggrephagy, ER-phagy, and mitophagy in the adult brain under basal conditions, as supported by the enrichment of their respective protein contents and #corresponding SARs.

### Characterization of brain autophagic degradome reveals selective autophagy pathways

We sought to characterize a validated brain autophagic degradome, defined as the portion of the brain's proteome that is

both present in LC3-pAVs and accumulates upon autophagy impairment. To this end, we established three experimental paradigms, where autophagy is either impaired genetically in the neural lineage or pharmacologically in brain slices and primary cell cultures (Figure S3A). For the genetic impairment, *atg5* was ablated under the *nestin-cre* promoter from early development (Figure S3B). *Atg5* levels are undetectable in *nestin-cre* (*nestin-cre;atg5<sup>fl/fl</sup>*) brain lysates, while the levels of non-lipidated LC3-I, Gabarapl2-I, and p62 are significantly increased as compared with *atg5<sup>fl/fl</sup>* controls, indicating the effective impairment of macroautophagy.<sup>10</sup> In the second paradigm, adult forebrain slices were maintained *ex vivo* for 3 h in the presence or absence of chloroquine (CQ), which sufficiently blocks autophagic flux, resulting in the accumulation of lipidated Atg8 proteins (Figure S3C). In the third paradigm, forebrain cultures were treated with Baf for 3 h to block autophagic flux, with or without a cocktail of SBI-0206965 and SAR405 (abbreviated as SS), for 6 h to block AV biogenesis (Figures S1F–S1K). We performed proteomic analyses of the three paradigms, employing three to five biological replicates per condition, which all correlated with a median Pearson coefficient of 0.989 (spread of 0.976–0.995; Figures S3D, S3F, and S3H). In all cases, PCAs could clearly separate experimental conditions (Figures S3E, S3G, and S3I).

When merging the degradomes validated in the three paradigms, we obtained 995 proteins that we coined combined brain degradomes (Table S5), constituting 34.3% of the LC3-pAV content. Cellular component analysis showed an enrichment for proteins localized to synapses, mitochondria, and intracellular vesicles (Figure S3J). This was further confirmed by comparison with the Human Protein Atlas, indicating the presence of synaptic-annotated (26.2%) and mitochondrial proteins (18.4%), followed by proteins localized in the ER (5.2%) and Golgi (4.3%) (Figure S3K).

### Figure 3. Brain autophagic degradome reveals constitutive aggrephagy

(A and B) Western blot of control and *nestin-cre* forebrain lysates for (A) Tax1bp1, p62, Alfy, and (B) K63-Ubiquitin.

(C) Graph shows the normalized levels of the indicated proteins in *nestin-cre* forebrain lysates expressed as a percentage of mean values of the control.  $n = 3$ , statistical analyses by unpaired t test. Tax1bp1:  $p = 0.0004$ ; p62:  $p < 0.0001$ ; K63-Ubiquitin:  $p = 0.0019$ ; and Alfy:  $p = 0.0037$ .

(D and E) Western blot for (D) p62 and Alfy and (E) K63-ubiquitin in neuronal lysates upon Baf, SS, or SS+Baf.

(F) Graph shows the normalized levels of the indicated proteins in the aforementioned conditions expressed as a percentage of control mean values.  $n = 4$ ; Alfy:  $F(3,12) = 8.899$ ;  $p = 0.0022$  (Tukey's multiple comparison test  $P_{ctrl\_Baf} = 0.0118$ ,  $P_{ctrl\_SS} = 0.0067$ , and  $P_{ctrl\_SS+Baf} = 0.0011$ ); p62:  $F(3,12) = 397.4$ ,  $p < 0.0001$  (Tukey's multiple comparison test  $P_{ctrl\_Baf} < 0.0001$ ,  $P_{ctrl\_SS} < 0.0001$ , and  $P_{ctrl\_SS+Baf} < 0.0001$ ); K63 ubiquitination:  $F(3,12) = 609.2$ ,  $p < 0.0001$  (Tukey's multiple comparison test  $P_{ctrl\_Baf} < 0.0001$ ,  $P_{ctrl\_SS} < 0.0001$ , and  $P_{ctrl\_SS+Baf} < 0.0001$ ).

(G–I) Representative images of (G) neurons, (H) astrocytes, and (I) oligodendrocytes, immunolabelled for p62 and cell-type-specific markers (MAP2: neurons; GFAP: astrocytes; and O4: oligodendrocytes) before and after treatment with Baf or SS. Scale bar, 10  $\mu$ m.

(J) Graph shows the number of normalized p62 puncta as a percentage of control mean values.  $n = 6$ , statistical analyses by one-way ANOVA. Neurons:  $F(2,15) = 26.54$ ,  $p < 0.0001$  (Tukey's multiple comparison test  $P_{ctrl\_Baf} = 0.0009$ , and  $P_{ctrl\_SS} < 0.0001$ ). Astrocytes:  $F(2,15) = 105.5$ ,  $p < 0.0001$  (Tukey's multiple comparison test  $P_{ctrl\_Baf} < 0.0001$  and  $P_{ctrl\_SS} < 0.0001$ ). Oligodendrocytes:  $F(2,15) = 7.229$ ,  $p < 0.0001$  (Tukey's multiple comparison test  $P_{ctrl\_Baf} = 0.0164$  and  $P_{ctrl\_SS} = 0.0058$ ).

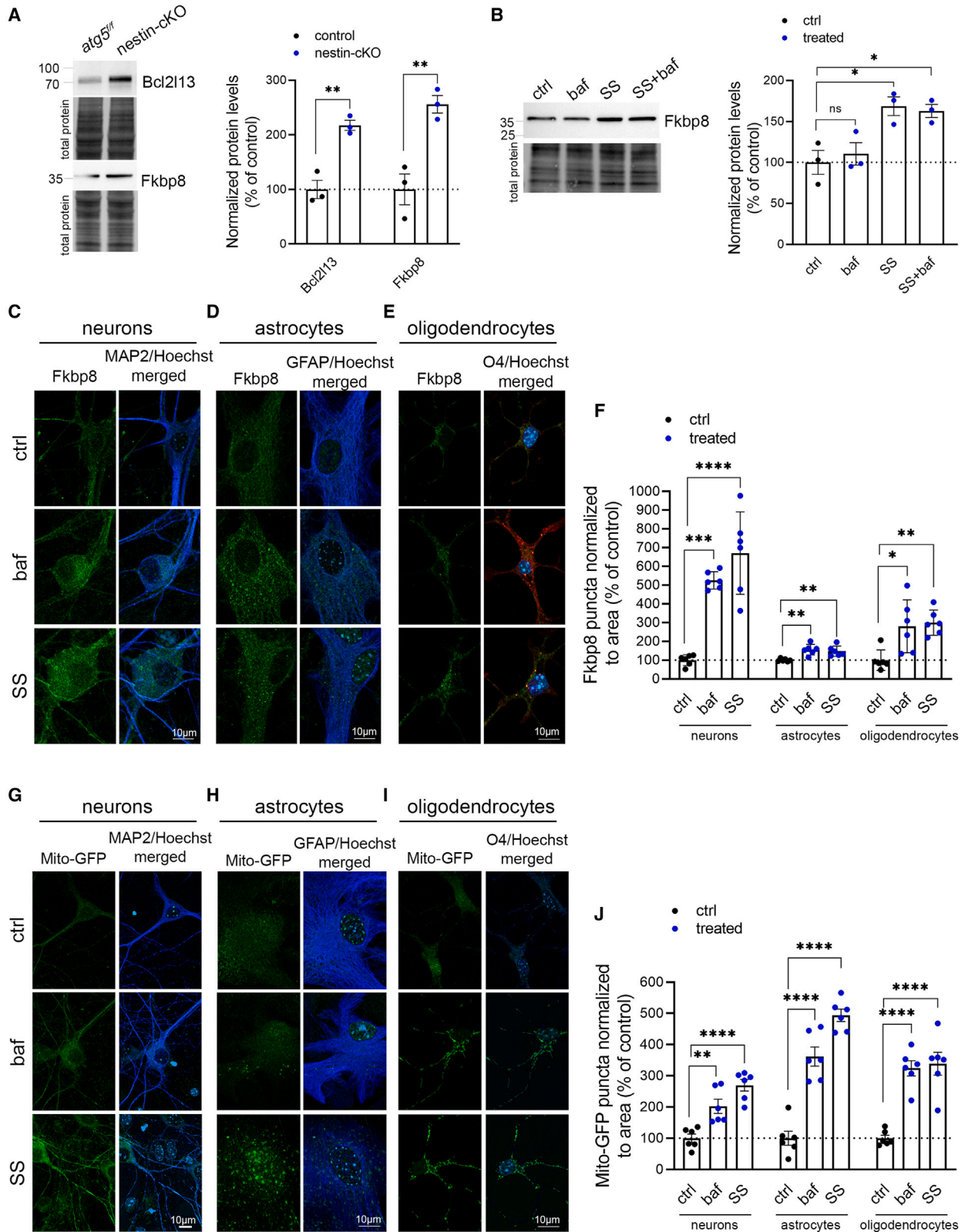
(K–M) Representative images of (K) neurons, (L) astrocytes, (M) oligodendrocytes immunolabelled for K63-ubiquitin, and cell-type-specific markers (neurofilament and MAP2: neurons, GFAP: astrocytes and O4: oligodendrocytes) before and after treatment with Baf or SS. Scale bar, 10  $\mu$ m.

(N) Graph shows the normalized number of K63-puncta as a percentage of control mean values.  $n = 6$ , statistical analyses by one-way ANOVA. Neurons:  $F(2,15) = 24.43$ ,  $p < 0.0001$  (Tukey's multiple comparison test  $P_{ctrl\_Baf} = 0.0006$  and  $P_{ctrl\_SS} < 0.0001$ ). Astrocytes:  $F(2,15) = 9.700$ ,  $p = 0.0020$  (Tukey's multiple comparison test  $P_{ctrl\_Baf} = 0.0016$  and  $P_{ctrl\_SS} = 0.0088$ ). Oligodendrocytes:  $F(2,15) = 67.81$ ,  $p < 0.0001$  (Tukey's multiple comparison test  $P_{ctrl\_Baf} < 0.0001$  and  $P_{ctrl\_SS} < 0.0001$ ).

(O and P) Representative images of microglia immunolabelled for (O) p62 or (P) K63-ubiquitin, the microglial marker P2Y12R and 4',6-diamidino-2-phenylindole (DAPI), before and after 6 h-treatment with SAR405 (1  $\mu$ M). Graphs show the % area covered by (O) p62 puncta or (P) K-63 puncta per cell, expressed as a fold-change of control mean values.  $n = 4$ , statistical analyses by unpaired t test, p62:  $p < 0.0001$ ; K-63:  $p = 0.0248$ . Scale bar, 10  $\mu$ m.

Baf: (BafilomycinA1, 50 nM, 3 h), SS: (SBI-0206965+SAR405, 3  $\mu$ M each, 6 h), SS+Baf: (SS: 3  $\mu$ M each, 6 h; Baf: 50 nM, last 3 h).

(C, F, J, N, O, and P) Bars represent mean values  $\pm$  SEM.



(legend on next page)

We examined whether SARs and their respective cargo were validated as degradomes. Regarding aggregophagy, Alf1, p62, and Tax1bp1 accumulated in the *nestin-cKO*, compared with controls (Figures 3A and 3C). Consistently, K63-ubiquitinated proteins also increased in the *nestin-cKO* (Figures 3B and 3C). K63-ubiquitinated proteins Alf1 and p62 both accumulated in the *in vitro* paradigm (Figures 3D–3F).

To examine whether aggregophagy takes place in different brain cells, we cultured neurons, astrocytes, oligodendrocytes, or microglia and monitored the accumulation of p62 and K63-ubiquitin after impairing the autophagic flux, or the biogenesis of AVs, by a 3-h treatment with Baf or a 6-h treatment with SS, respectively. In microglia, AV biogenesis was blocked by a 6-h treatment with SAR405 alone, which was well-tolerated. Treatments resulted in a significant accumulation of p62 puncta and K63-ubiquitin across all cell types (Figures 3G–3P). In neurons, the accumulation was perinuclear, not affecting neurites marked by MAP2 (dendrites) nor neurofilament (axons) (Figures 3G and 3K).

The combined brain degradome contained two mitophagy SARs, Fkbp8 and Bcl2l13 (Table S5), which accumulated in *nestin-cKO* forebrain lysates, compared with control (Figure 4A). Fkbp8 levels also increased in forebrain cultures treated with SS (Figure 4B). Next, we performed immunocytochemistry for Fkbp8 in cultured neurons (Figures 4C and 4F), astrocytes (Figures 4D and 4F), and oligodendrocytes (Figures 4E and 4F) and found a significant accumulation in all cell types both when AV biogenesis and flux are blocked. However, Fkbp8 failed to accumulate in microglia treated with SAR405 (Figure S4A), suggesting that mitophagy may not occur constitutively under basal conditions via this receptor.

We then examined the mitochondrial content of neurons, astrocytes, and oligodendrocytes transduced with a construct encoding GFP fused to the leader sequence of the mitochondrial matrix protein, E1 alpha pyruvate dehydrogenase (Mito-GFP). All cells exhibited increased GFP fluorescence upon Baf or SS treatment, which also appeared more punctate (Figures 4G–4J). In neurons, increased fluorescence predominated in the somatodendritic area (Figure 4G) as well as in axons (Figure S4B),

while in astrocytes and oligodendrocytes it was widespread (Figures 4H and 4I). Furthermore, 182 mitochondrial proteins (comprising 27% of the mitochondrial LC3-pAV content) were found in the degradome, significantly accumulating in one or more paradigms of autophagy impairment (Table S5; Figure S4C). The mitochondrial degradome showed enrichment for the electron transport chain, cellular respiration, and mitochondrial organization processes (Figure S4D).

Moreover, all ER-phagy receptors (Calcoco1, Rtn3, Fam134a, and At13) were found in the brain degradome, accumulating in one or more autophagy impairment paradigms (Table S5). At13 accumulated in cultures upon SS treatment (Figure 5A) and in *nestin-cKO* forebrain lysates, compared with controls (Figure 5A). Similarly, isoforms 1, 2, 3, and 4 of Rtn3 significantly increased in *nestin-cKO* forebrains, as compared with controls (Figure 5B), while isoform 5 significantly increased in CQ-treated brain slices (Figure 5B). We then immunolabelled cultured cells for Rtn3 before and after blockage of the AV biogenesis (SS) and flux (Baf). Although Rtn3 exhibited low expression under control conditions, both Baf and SS caused its perinuclear accumulation in all cell types (Figures 5C–5F). Neuronal Rtn3 also profoundly increased in axonal processes, marked by neurofilaments (Figure S5A). Rtn3 also accumulated significantly in cultured microglia treated with SAR405 (Figure S5B).

We examined the ER content in brain cells transduced with GFP fused to the ER signal sequences of calreticulin and KDEL (ER retention signal). Both Baf and SS treatments resulted in a significant increase in punctate GFP signals across cells (Figures 5G–5I), which also resembled ER fragmentation within astrocytes (Figure 5H).

Consistently, 41.3% of the ER and 30.9% of the Golgi LC3-pAV content was found in the combined brain degradome (Table S5) and their localization is depicted in Figure S5C. Further analysis revealed an enrichment for proteins involved in ER organization and vesicular transport (Figure S5D). The brain ER-Golgi degradome includes previously identified ER-autophagy substrates in neurons,<sup>14</sup> such as Rtn4, Vapa, Calu, Tecr, and Sac1, whose accumulation was biochemically confirmed in our autophagy impairment paradigms (Figures 5K and 5L).

#### Figure 4. Brain autophagic degradome reveals constitutive mitophagy

(A) Western blot of forebrain lysates from control and *nestin-cKO* mice for Bcl2l13 and Fkbp8. Graph shows their normalized levels expressed as a percentage of control mean values.  $n = 3$ , statistical analyses by unpaired t test. Bcl2l13:  $p = 0.0035$ , Fkbp8:  $p = 0.0084$ .

(B) Western blot of forebrain culture lysates for Fkbp8 before and after treatment with Baf, SS or SS+Baf. Graph shows the normalized levels of Fkbp8 as percentage of control mean values.  $n = 3$ , statistical analyses by one-way ANOVA.  $F(3,8) = 8.388$   $p = 0.0075$  (Tukey's multiple comparison test  $P_{ctrl\_Baf} = 0.9267$ ,  $P_{ctrl\_SS} = 0.0170$ , and  $P_{ctrl\_SS+Baf} = 0.0269$ ).

(C–E) Representative images of (C) neurons, (D) astrocytes and (E) oligodendrocytes, immunolabelled for Fkbp8 and cell-type-specific markers (MAP2: neurons, GFAP: astrocytes, and O4: oligodendrocytes) before and after treatment with Baf or SS. Scale bar, 10  $\mu$ m.

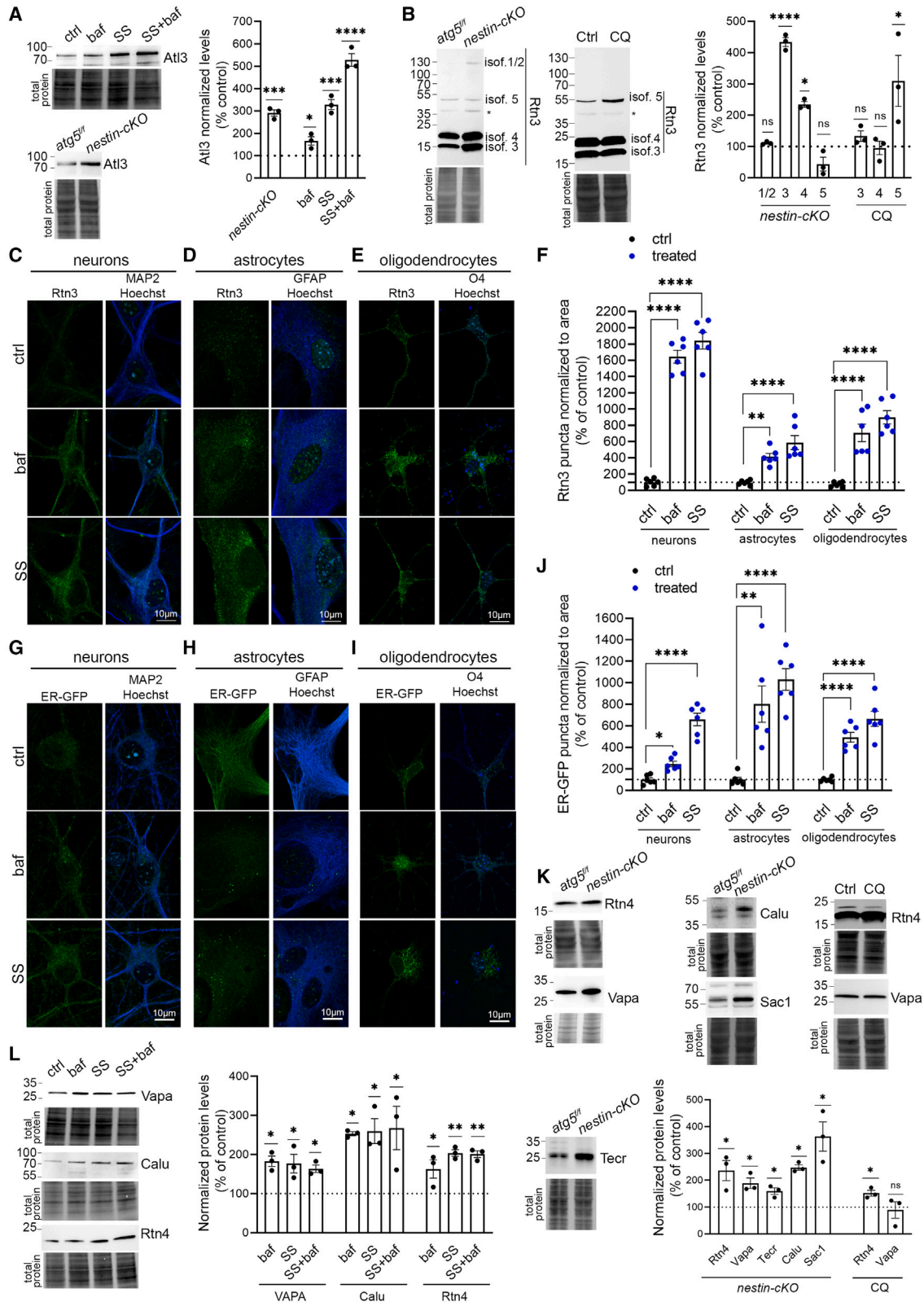
(F) Graph shows the normalized number of Fkbp8 puncta as percentage of control mean values.  $n = 6$ , statistical analyses by one-way ANOVA. Neurons:  $F(2,15) = 30.84$   $p < 0.0001$  (Tukey's multiple comparison test  $P_{ctrl\_Baf} = 0.0001$  and  $P_{ctrl\_SS} < 0.0001$ ). Astrocytes:  $F(2,15) = 10.29$   $p = 0.0015$  (Tukey's multiple comparison test  $P_{ctrl\_Baf} = 0.0021$  and  $P_{ctrl\_SS} = 0.0071$ ). Oligodendrocytes:  $F(2,15) = 7.971$   $p = 0.0044$  (Tukey's multiple comparison test  $P_{ctrl\_Baf} = 0.0135$  and  $P_{ctrl\_SS} = 0.0067$ ).

(G–I) Representative images of CellLight Mito-GFP signal in (G) neurons, (H) astrocytes, and (I) oligodendrocytes, before and after treatment with Baf or SS. Scale bar, 10  $\mu$ m.

(J) Graph shows the normalized number of Mito-GFP puncta as percentage of the control mean values.  $n = 6$ , statistical analyses by one-way ANOVA. Neurons:  $F(2,15) = 21.03$ ,  $p < 0.0001$  (Tukey's multiple comparison test  $P_{ctrl\_Baf} = 0.0040$  and  $P_{ctrl\_SS} < 0.0001$ ). Astrocytes:  $F(2,15) = 65.03$ ,  $p < 0.0001$  (Tukey's multiple comparison test  $P_{ctrl\_Baf} < 0.0001$  and  $P_{ctrl\_SS} < 0.0001$ ). Oligodendrocytes:  $F(2,15) = 26.28$ ,  $p < 0.0001$  (Tukey's multiple comparison test  $P_{ctrl\_Baf} < 0.0001$  and  $P_{ctrl\_SS} < 0.0001$ ).

Baf: (BafilomycinA1, 50 nM, 3 h), SS: (SBI-0206965+SAR405, 3  $\mu$ M each, 6 h).

(A, B, F, and J) Bars represent mean values  $\pm$  SEM.



(legend on next page)

Rtn4 levels significantly increased in all paradigms, while Vapa increased in the genetic and *in vitro* paradigms, but not in the *ex vivo* paradigm, consistent with the proteomic analyses (Figures 5K and 5L). Sac1 and Tecr exhibited increased levels in the *nestin-cKO* paradigm (Figure 5K), whereas Calu increased in both the *nestin-cKO* and *in vitro* paradigm (Figures 5K and 5L).

Taken together, our findings support the constitutive turnover of aggregates, mitochondria, and ER-Golgi across different brain cells by autophagy, via the identified and degradome-validated SARs.

Synaptic proteins (273 proteins, 41.8% of LC3-pAV synaptic-annotated content) comprise a quarter of the combined brain degradome (Figure S3G). Their distribution at the synapse is schematically represented in Figure 6A. They include the presynaptic active zone proteins Piccolo (Pclo) and Bassoon (Bsn), the postsynaptic anchors Shank3 and Dlgap4, and glutamate receptor subunits such as Grin1, Grin2b, and Gria2. As a proof of concept, some of these proteins were confirmed biochemically to accumulate in autophagy-impaired conditions (Figures 6B–6D). Consistent with the proteomic analyses, the glutamate receptor subunits Gria2, Grin1, and Grin2b accumulated in cultured neurons upon impairment of AV biogenesis (SS) and flux (Baf) (Figure 6B). Similarly, Grin1 also accumulated in brain slices incubated *ex vivo* with CQ to block the autophagic flux (Figures 6C and 6D). In the same condition, we confirmed the accumulation of several other proteins: Shank3, a key synaptic scaffold; Syt7, involved in synaptic vesicle release; Dynamin1, involved in endocytosis at synaptic membranes; and Rims1, which regulates neurotransmitter release (Figures 6C and 6D). The key active zone regulator, Bassoon, was also among the degradome and significantly accumulated in puncta juxtaposing MAP2-labeled dendrites upon impaired AV biogenesis (SS)

and flux (Baf) (Figure 6E). Biological process analysis indicated that the synaptic degradome is enriched for functions in vesicle-mediated transport in the synapse, synaptic organization, and trans-synaptic signaling (Figure 6F). To gain insight into how synaptic proteins are recruited to phagophores, we assessed the presence of LC3-interacting region (LIR) motifs<sup>36–38</sup> using a prediction tool.<sup>39</sup> We found that 47.2% contain one or more WxxL-predicted LIR motifs, 49.3% contain at least one xLIR motif, while only 3.5% do not contain any predicted motif (Figure 6G). The number and sequences of LIR motives are summarized in Table S6.

Taken together, our unbiased analyses demonstrate the autophagic turnover of key synaptic proteins involved in basal neurotransmission and neuronal excitability.

### The brain LC3-pAV content and degradome are temporally regulated

To gain insight into the temporal and developmental dynamics of autophagic degradation, we compared the LC3-pAV content of adolescent, adult, and aged brains. Biological replicates correlated well with a median Pearson coefficient of 0.93 (Figure S6A, Pearson coefficient 0.86–0.97).

In comparing adult and aged brains, the weight of LC3-pAVs per mg was comparable between the two ages. Therefore, we wondered whether there were instead qualitative differences in the content. We quantitatively compared the adult and aged LC3-pAV contents (Figure S6B) but found no major differences between the two ages (Table S7). Only 48 proteins were enriched in aged (Figure S6C) and 65 proteins in adult LC3-pAVs (Figure S6D), respectively. Most LC3-pAV content proteins showed comparable expression levels in forebrain whole-cell lysates from the two ages (Figure S6E; Table S8). Biological process enrichment analysis of

### Figure 5. Brain autophagic degradome reveals constitutive ER-phagy

(A) Western blot for Atf3 in forebrain culture lysates upon Baf, SS, or SS+Baf, and in control and *nestin-cKO* forebrain lysates. Graph shows normalized Atf3 levels as percentage of control mean values.  $n = 3$ , statistical analysis for cultures by one-way ANOVA.  $F(3,8) = 86.76$ ,  $p < 0.0001$  (Tukey's multiple comparison test  $P_{ctrl\_Baf} = 0.0723$ ,  $P_{ctrl\_SS} = 0.0001$ , and  $P_{ctrl\_SS+Baf} < 0.0001$ ); for *nestin-cKO*s by unpaired t test. Atf3:  $p = 0.0002$ .

(B) Western blot for Rtn3 in control and *nestin-cKO* forebrain lysates and in forebrain slice-lysates before or after CQ treatment. Graph shows the normalized Rtn3 levels as percentage of control mean values.  $n = 3$ , statistical analyses by unpaired t test. For *nestin-cKO*:  $Rtn3_{isoform1/2}$ :  $p = 0.0940$ ,  $Rtn3_{isoform3}$ :  $p < 0.0001$ ,  $Rtn3_{isoform4}$ :  $p = 0.0153$ ,  $Rtn3_{isoform5}$ :  $0.3693$ . For CQ treatment:  $Rtn3_{isoform3}$ :  $p = 0.3696$ ,  $Rtn3_{isoform4}$ :  $p = 0.8786$ ,  $Rtn3_{isoform5}$ :  $0.0162$ .

(C–E) Representative images of (C) neurons, (D) astrocytes, and (E) oligodendrocytes, immunolabelled for Rtn3, cell-type-specific markers (MAP2:neurons, GFAP: astrocytes, and O4: oligodendrocytes) and Hoechst, before and after Baf or SS. Scale bar, 10  $\mu$ m.

(F) Graph shows the normalized number of Rtn3 puncta as percentage of control mean values.  $n = 6$ , statistical analyses by one-way ANOVA. Neurons:  $F(2,15) = 159.0$ ,  $p < 0.0001$  (Tukey's multiple comparison test  $P_{ctrl\_Baf} < 0.0001$  and  $P_{ctrl\_SS} < 0.0001$ ). Astrocytes:  $F(2,15) = 20.41$ ,  $p < 0.0001$  (Tukey's multiple comparison test  $P_{ctrl\_Baf} = 0.0019$  and  $P_{ctrl\_SS} < 0.0001$ ). Oligodendrocytes:  $F(2,15) = 30.34$ ,  $p < 0.0001$  (Tukey's multiple comparison test  $P_{ctrl\_Baf} < 0.0001$  and  $P_{ctrl\_SS} < 0.0001$ ).

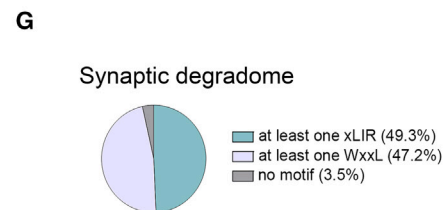
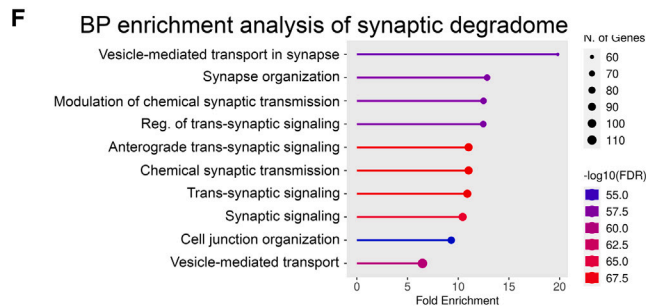
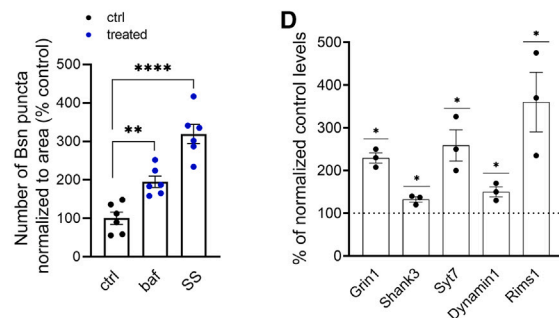
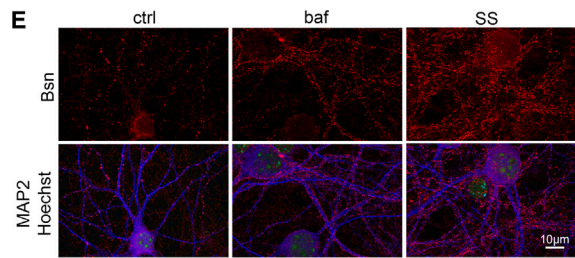
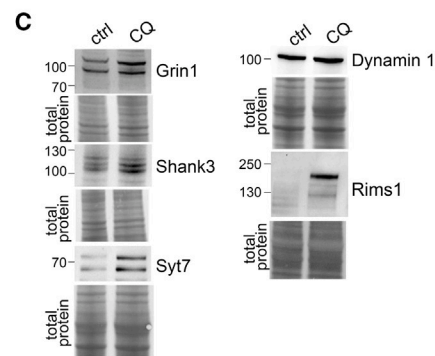
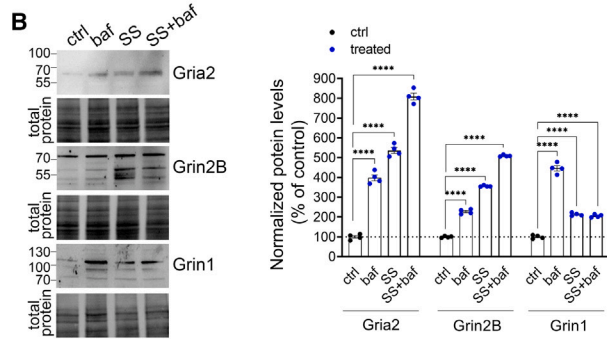
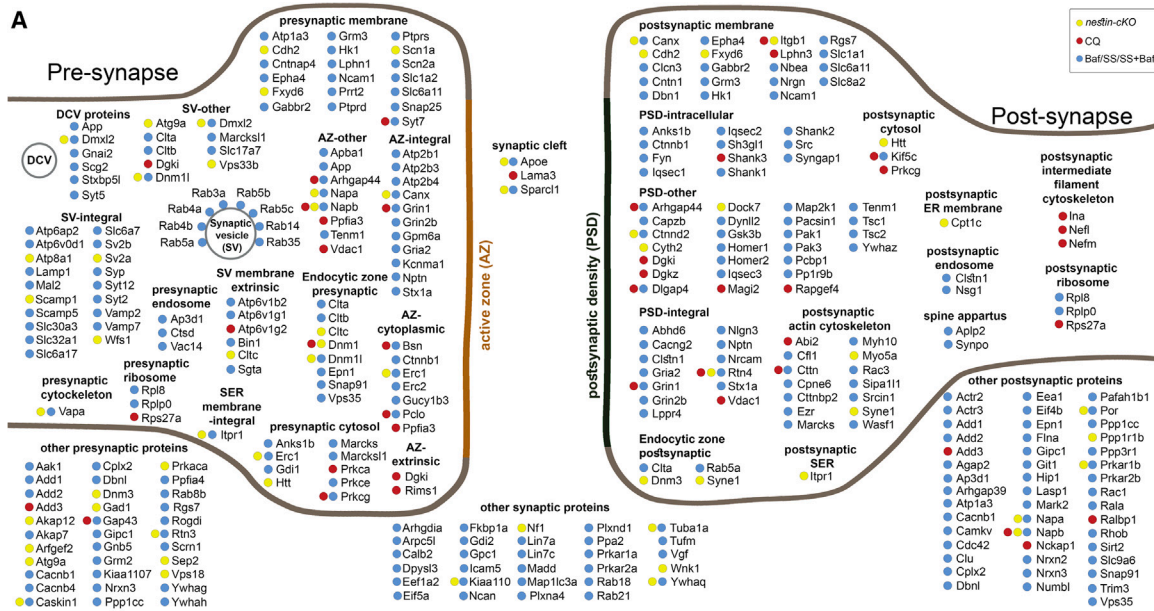
(G–I) Representative images of the CellLight ER-GFP signal in (G) neurons, (H) astrocytes, and (I) oligodendrocytes before and after Baf or SS. Scale bar, 10  $\mu$ m.

(J) Graph shows the normalized number of ER-GFP puncta as percentage of control mean values.  $n = 6$ , statistical analyses by one-way ANOVA. Neurons:  $F(2,15) = 59.00$ ,  $p < 0.0001$  (Tukey's multiple comparison test  $P_{ctrl\_Baf} = 0.0287$  and  $P_{ctrl\_SS} < 0.0001$ ). Astrocytes:  $F(2,15) = 18.06$ ,  $p = 0.0001$  (Tukey's multiple comparison test  $P_{ctrl\_Baf} = 0.0011$  and  $P_{ctrl\_SS} < 0.0001$ ). Oligodendrocytes:  $F(2,15) = 35.36$ ,  $p < 0.0001$  (Tukey's multiple comparison test  $P_{ctrl\_Baf} < 0.0001$  and  $P_{ctrl\_SS} < 0.0001$ ).

(K) Western blot for Rtn4, Vapa, Calu, and Sac1 in control and *nestin-cKO* forebrain lysates, and for Rtn4 and Vapa in forebrain slice lysates before or after CQ treatment. Graph shows the normalized levels of these proteins as percentage of control mean values.  $n = 3$ , statistical analyses by unpaired t test. *nestin-cKO*: Rtn4:  $p = 0.0242$ , Vapa:  $p = 0.0153$ , Tecr:  $p = 0.0223$ , Calu:  $p = 0.0133$ , Sac1:  $p = 0.0142$ . CQ treatments: Rtn4:  $p = 0.0191$  and Vapa:  $p = 0.7598$ .

(L) Western blot for Vapa, Calu, and Rtn4 in forebrain slice lysates after CQ treatment and for Vapa in forebrain culture lysates before or after Baf, SS, or SS+Baf. Graph shows the normalized levels of these proteins as percentage of control mean values.  $n = 3$ , statistical analyses by one-way ANOVA. Vapa:  $F(3,8) = 6.022$ ,  $p = 0.0190$  (Tukey's multiple comparison test  $P_{ctrl\_Baf} = 0.0136$ ,  $P_{ctrl\_SS} = 0.0203$ , and  $P_{ctrl\_SS+Baf} = 0.0484$ ). Calu:  $F(3,8) = 5.929$ ,  $p = 0.0198$  (Tukey's multiple comparison test  $P_{ctrl\_Baf} = 0.0277$ ,  $P_{ctrl\_SS} = 0.0225$ , and  $P_{ctrl\_SS+Baf} = 0.0177$ ), and Rtn4:  $F(3,8) = 9.877$ ,  $p = 0.0046$  (Tukey's multiple comparison test  $P_{ctrl\_Baf} = 0.0495$ ,  $P_{ctrl\_SS} = 0.0036$ , and  $P_{ctrl\_SS+Baf} = 0.0043$ ).

Baf: (BafilomycinA1, 50 nM, 3 h), SS: (SBI-0206965+SAR405, 3  $\mu$ M each, 6 h), SS+Baf: (SS: 3  $\mu$ M each, 6 h; Baf: 50 nM, last 3 h), CQ: (Chloroquine, 100  $\mu$ M, 3 h). (A, B, F, J, K, and L) Bars represent mean values  $\pm$  SEM.



differentially abundant LC3-pAV proteins revealed an enrichment for tRNA biosynthesis, myosin filament organization, and cellular catabolic processes in the aged brain (Figure S6F).

By contrast, major differences were observed in the comparisons with the adolescent stage. The adolescent LC3-pAV content showed enrichment for 167 (Figures 7A and 7B) and 115 proteins (Figures 7E and 7F) when compared with the adult and the aged content, respectively (Table S9). In both comparisons, most adolescent-enriched LC3-pAV proteins were mitochondrial (Figures 7D, 7H, and 7I), including two mitophagy receptors, Fkbp8 and Phb2. Western blot analysis of forebrain slices treated *ex vivo* with CQ indicated increased flux of Phb2 in the adolescent brain as compared with the adult brain (Figure 7J). Adolescent-enriched mitochondrial substrates were enriched in functions in fatty acid beta oxidation and mitochondrial translation (Figures 7D and 7H). Moreover, 32% of the differentially enriched LC3-pAV mitochondrial proteins were validated as brain degradomes (asterisks in Figure 7I). Proteomic comparison of these mitochondrial proteins in adolescent, adult, and aged brain lysates indicated that most showed similar expression levels between ages (Figure S6G). Therefore, mitophagy may be enhanced in the adolescent brain compared with the adult and aged stages, as supported by the enrichment of the adolescent LC3-pAV content for mitochondrial proteins, including mitophagy receptors.

Conversely, the adult and aged LC3-pAV contents were enriched for 438 (Figure 7C) and 312 proteins (Figure 7G), respectively, compared with those in adolescence. Notably, ER and Golgi autophagic substrates were mostly enriched in the adult and aged content, as schematically represented in Figure 7K. Western blot analysis of brain slices treated *ex vivo* with CQ further indicated increased flux of Rab1b, an ER substrate, in the adult brain, as compared with the adolescent brain (Figure 7L).

Moreover, a large portion of both the adult- and aged-enriched LC3-pAV content was composed of synaptic proteins (Figures 7C and 7G), with functions in the synaptic vesicle cycle, synaptic transmission, and trans-synaptic signaling (Figures 7D and 7H) and widespread pre- and postsynaptic localizations (Figure 8A). Moreover, 39.3% of these proteins were validated as synaptic degradomes (asterisks in Figure 8A). The vast majority exhibited similar expression levels across ages (Table S10), with the exception of very few (Figure 8B).

Consistently, N-methyl-D-aspartate (NMDA) receptor subunit NR1 (Grin1) was more abundant in PK-treated LC3-pAVs from adult brains as compared with those from adolescent brains (Figure 8C). Grin1 also accumulated in adult brain slices upon CQ treatment *ex vivo*, as compared with adolescent slices (Figure 8D). In the same paradigm, inositol-trisphosphate 3-kinase A (Itpka), a component of the postsynaptic actin cytoskeleton, also accumulated significantly more in adult brain slices as compared with adolescent ones (Figure 8D), consistent with the proteomic analyses (Figure 8A).

By contrast, only 27 synaptic proteins were enriched in the adolescent LC3-pAV content, which mainly localized to the postsynaptic membrane and synaptic ribosome (green circles in Figure 8A, degradome denoted by asterisks). Finally, only 14 proteins were significantly enriched in the adult LC3-pAV content as compared with the aged group. One of them, alpha-internexin (Ina), a neuronal intermediate filament protein, was confirmed to accumulate significantly more in CQ-treated adult brain slices as compared with the aged ones (Figure 8E).

The sequestration of synaptic proteins into AVs seems generally enhanced in the adult and aged brains as compared with the adolescent brain. The only exception is the sequestration of selected postsynaptic membrane and postsynaptic ribosome proteins at adolescence, which may signify autophagy's contribution to developmental spine pruning, as previously described.

Overall, these findings demonstrate that the LC3-pAV content is progressively dynamic from adolescence to aging, whereas it remains largely stable between the adult and aged brains. They also indicate that mitophagy and synaptic protein turnover are regulated in opposite ways, progressively represented in young and matured brains, respectively.

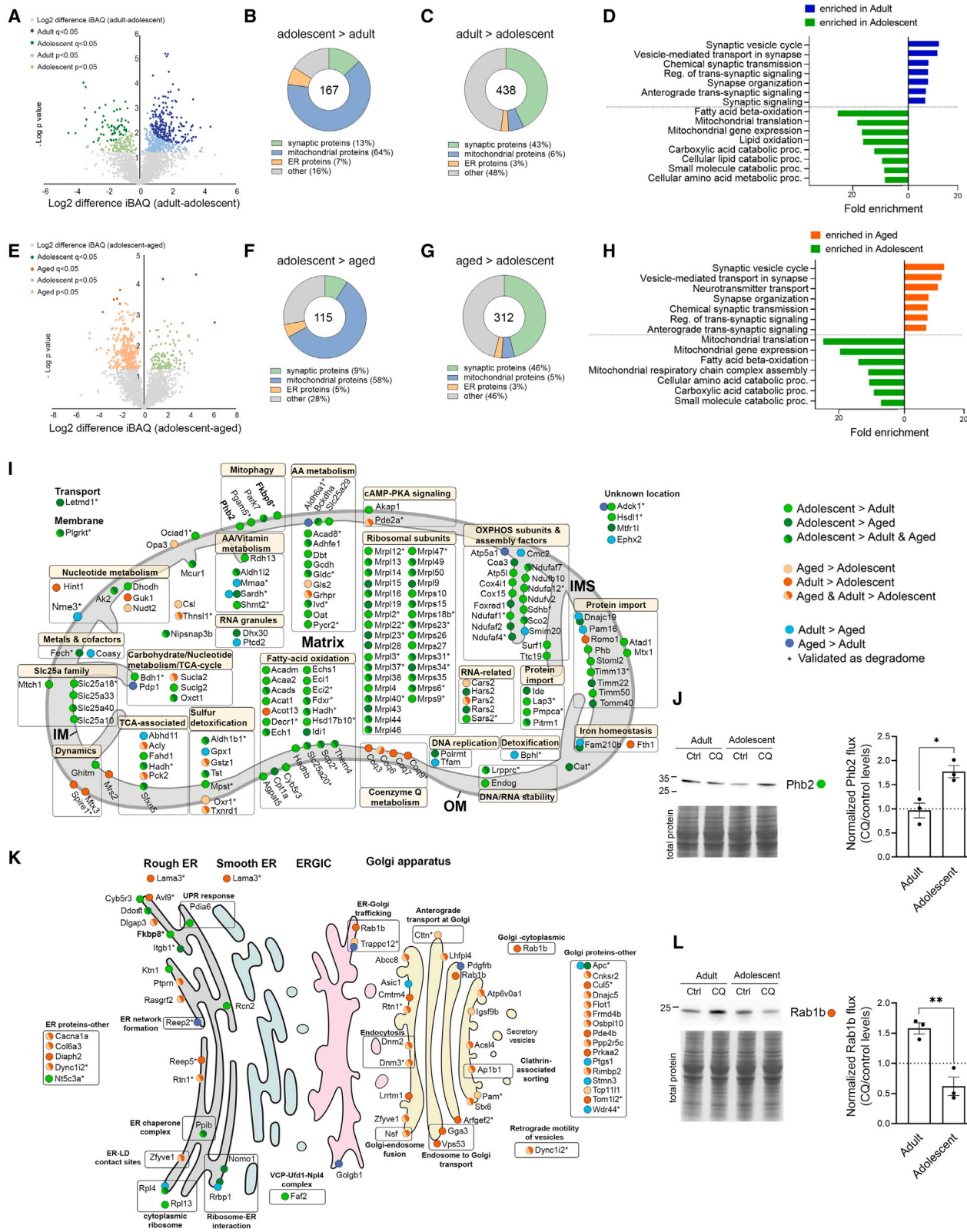
## DISCUSSION

To gain insight into the autophagic turnover of brain constituents, we established a two-step method to immunopurify brain AVs. This approach allowed us to overcome the shortcomings associated with impure brain AV-enriched fractions, whose previous profiling did not reveal selective autophagy pathways.<sup>28</sup>

As our method relies on LC3-dependent purification, we opted to exclude the possibility of enriching for other vesicles with

### Figure 6. Synaptic-annotated brain degradome

- (A) Schematic of the topology and function of synaptic-annotated brain degradome proteins. Color-coded circle(s) denote the paradigm(s) of accumulation.
- (B) Western blot for Gria2, Grin2b, and Grin1 in forebrain culture lysates before or after Baf, SS or SS+Baf. Graph shows the normalized levels of these proteins as percentage of control mean values.  $n = 4$ , statistical analyses by one-way ANOVA. Gria2:  $F(3,12) = 446.3$ ,  $p < 0.0001$  (Tukey's multiple comparison test  $P_{\text{ctrl\_Baf}} < 0.0001$ ,  $P_{\text{ctrl\_SS}} < 0.0001$ , and  $P_{\text{ctrl\_SS+Baf}} < 0.0001$ ), Grin2b:  $F(3,12) = 2,612$ ,  $p < 0.0001$  (Tukey's multiple comparison test  $P_{\text{ctrl\_Baf}} < 0.0001$ ,  $P_{\text{ctrl\_SS}} < 0.0001$ , and  $P_{\text{ctrl\_SS+Baf}} < 0.0001$ ), and Grin1:  $F(3,12) = 385.7$ ,  $p < 0.0001$  (Tukey's multiple comparison test  $P_{\text{ctrl\_Baf}} < 0.0001$ ,  $P_{\text{ctrl\_SS}} < 0.0001$ , and  $P_{\text{ctrl\_SS+Baf}} < 0.0001$ ).
- (C) Western blot for Grin1, Shank3, Syt7, Dymanin1, and Rims1 in forebrain slice lysates before or after CQ treatment.
- (D) Graph shows the normalized levels of these proteins, expressed as percentage of control mean values.  $n = 3$ , statistical analyses by unpaired t test. Grin1:  $p = 0.0162$ , Shank3:  $p = 0.0138$ , Syt7:  $p = 0.0484$ , Dynamin1:  $p = 0.0199$ , Rims1:  $p = 0.0221$ .
- (E) Representative images of neurons immunolabelled for Bassoon (Bsn), MAP2 and Hoechst, before or after Baf or SS treatment.  $n = 6$ , statistical analyses by one-way ANOVA. Bsn puncta:  $F(2,15) = 33.00$ ,  $p < 0.0001$  (Tukey's multiple comparison test  $P_{\text{ctrl\_Baf}} = 0.0085$ ,  $P_{\text{ctrl\_SS}} < 0.0001$  and). Scale bar, 10  $\mu\text{m}$ .
- (F) Biological process enrichment analysis of synaptic-annotated degradome. Size and color of bubbles represent number of genes and enrichment significance, respectively.
- (G) Pie chart shows the percentage of synaptic-annotated degradome with at least one xLIR or WxxL motif.
- Baf: (BafilomycinA1, 50 nM, 3 h), SS: (SBI-0206965+SAR405, 3  $\mu\text{M}$  each, 6 h), SS+Baf:(SS: 3  $\mu\text{M}$  each, 6 h; Baf: 50 nM, last 3 h), CQ: (Chloroquine, 100  $\mu\text{M}$ , 3 h). (B, D, and E) Bars represent mean values  $\pm$  SEM.



(legend on next page)

non-canonical lipidation of LC3. Non-canonical LC3 lipidation was recently implicated in the phagocytic efficiency of microglia in an Alzheimer's disease model, where the clearing of A $\beta$  plaques was dependent on LANDO,<sup>40,41</sup> the non-canonical lipidation of LC3 on endosomes.<sup>42,43</sup> In neurons and astrocytes, we found that most LC3 lipidation occurs on autophagic membranes, as it is suppressed by inhibition of ULK1, a kinase required for AV biogenesis (Figures S1F–S1K). Consistently, electron tomography of the immunoprecipitated material showed strong enrichment (87.8%) for AVs (Figures 1E and 1F), which are intact and fit for fusion with lysosomes.<sup>3</sup> Therefore, we postulate that in most brain cells, canonical lipidation of LC3 predominates. Few AVs remained in the LC3-IP unbound material, representing either fusion-ready vesicles where LC3 is cleaved-off or a subpopulation that does not present LC3 on their surface.

Here, we performed three unbiased proteomic analyses: (1) of the LC3-pAV content from three brain ages, (2) total protein expression from three brain ages, and (3) total protein expression from brains or cells with impaired autophagy. Combining this information, we not only compare the content of brain AVs at critical periods of maturation but also describe the portion of this content that is validated as a degradome, based on its accumulation upon autophagy impairment. We provide solid evidence for the basal turnover of protein aggregates, mitochondria, and ER, and identify the SARs involved in their sequestration. Some of these SARs were never associated with brain autophagy, while others, such as Tax1bp1, have been described either in basal conditions or in diseases.<sup>44–48</sup>

Our findings suggest that basal brain mitophagy is independent of PINK1 and Parkin and instead facilitated by other SARs, such as Fkbp8. This is consistent with recent findings using the mito-QC reporter mouse<sup>49</sup> and cultured neurons,<sup>50</sup> showing that PINK1 and Parkin are dispensable for basal mitophagy in brain cells. It is plausible that different mitophagy receptors are recruited under physiological or pathological states, given the implication of Pink-Parkin-dependent mitophagy in

neurodegenerative diseases.<sup>51</sup> The recent profiling of a brain AV-enriched fraction suggested a selective degradation of mitochondrial nucleoids instead of classical mitophagy.<sup>28</sup> Although we identify six of the twelve mitochondrial-nucleoid-associated proteins, the mitochondrial LC3-pAV degradome exhibits widespread functions and localizations. Hence, we have no evidence that mitochondrial nucleoids represent separate entities and postulate that they are part of the sequestered mitochondria.

Moreover, our findings elucidate the presence of basal ER-phagy in the brain, supporting recent evidence for the turnover of ER proteins by autophagy at excitatory axon terminals and its importance in basal neurotransmission.<sup>14</sup> There are seven well-described ER-phagy SARs from studies in non-brain cells: Fam134b, Rtn3, Ccpg1, Sec62, Tex264, Atf3,<sup>52</sup> and Calcoco1.<sup>53,54</sup> Here, we identify Atf3, Rtn3, Fam134a, and Calcoco1 as brain ER-phagy receptors. In addition, Fam134a, recently shown to act as an ER-phagy receptor under stress in cultured embryonic fibroblasts,<sup>35</sup> emerges as a potential basal brain ER-phagy receptor. By contrast, the well-characterized Fam134b receptor<sup>55</sup> is absent from the brain LC3-pAV content. In line with this, mutations in Fam134b cause sensory and autonomic neuropathies, sparing the brain.<sup>56</sup>

Aggrephagy has been mostly studied in disease-related contexts, largely focusing on p62. Here, we show that aggrephagy occurs constitutively under basal conditions, facilitated by three additional receptors, Tax1bp1, Tollip, and Alf1. Notably, Goldsmith and colleagues did not report any aggrephagy or ER-phagy SARs as part of their content.<sup>28</sup> We believe that these selective autophagy pathways were revealed by the purity of our preparation. An alternative explanation may be our focus on the forebrain, whereas Goldsmith and colleagues analyzed the whole brain. It is plausible that aggrephagy and ER-phagy are more prominent in the forebrain, which is enriched in glutamatergic neurons, as opposed to brain areas with greater cellular heterogeneity.

Conducive to the emerging role of autophagy as a key regulator of synaptic function, a quarter of the LC3-pAV content is composed of synaptic proteins, and just under half (41.8%) of

### Figure 7. Regulation of mitophagy and ER-phagy during brain maturation and aging

- (A) Volcano plot of differentially enriched proteins (t test,  $p$  or  $q < 0.05$ ) in adult or adolescent LC3-pAVs ( $n = 3$ ). iBAQ protein abundances were  $\log_2$  transformed and normalized to the median of the respective experiment.
- (B) Donut chart showing the percentage of the synaptic, mitochondrial, and ER proteins enriched in adolescent LC3-pAV content.
- (C) Donut chart showing the percentages of the synaptic, mitochondrial, and ER proteins enriched in adult pAV content.
- (D) Biological process enrichment analysis of the 605 dynamically regulated proteins between adolescent and adult LC3-pAVs.
- (E) Volcano plot of the differentially enriched proteins (t test,  $p$  or  $q < 0.05$ ) in aged or adolescent LC3-pAVs ( $n = 3$ ). iBAQ protein abundances were  $\log_2$  transformed and normalized to the median of the respective experiment.
- (F) Donut chart showing the percentage of the synaptic, mitochondrial and ER proteins found enriched in adolescent (vs. aged) LC3-pAV content, as parts of the 115 adolescent-enriched total proteins.
- (G) Donut chart showing the percentage of synaptic, mitochondrial and ER proteins found enriched in aged (vs adolescent) pAV content, as parts of the total 312 aged-enriched proteins.
- (H) Biological Process enrichment analysis of the 427 dynamically regulated proteins between adolescent and aged LC3-pAVs.
- (I) Schematic showing the topology and function of differentially abundant contents. Color-coded circles denote the differential abundance in age comparisons. Degradome proteins are denoted by an asterisk. AA: amino acid, OXPHOS: oxidative phosphorylation, TCA: trichloroacetic acid.
- (J) Western blot for Phb2 in adult or adolescent forebrain slice lysates upon CQ treatment. Graph shows the normalized flux of Phb2 in adult and adolescent samples, calculated as the CQ/control normalized signal ratio.  $n = 3$ , statistical analyses by unpaired t test ( $p = 0.0150$ ).
- (K) Schematic of the differentially abundant ER/Golgi proteins in adolescent, adult, or aged LC3-pAVs. Color-coded circles denote the age comparisons. Degradome proteins are denoted by an asterisk. ER: endoplasmic reticulum, ERGIC: ER-Golgi intermediate compartment.
- (L) Western blot for Rab1b in adult or adolescent forebrain slice lysates before or after CQ treatment. Graph shows the normalized flux of Rab1b in the adult and adolescent samples, calculated as the CQ/control normalized signal ratio.  $n = 3$ , statistical analyses by unpaired t test ( $p = 0.0060$ ).
- Baf: (BafilomycinA1, 50 nM, 3 h), SS: (SBI-0206965+SAR405, 3  $\mu$ M each, 6 h), SS+Baf: (SS: 3  $\mu$ M each, 6 h; Baf: 50 nM, last 3 h), CQ: (Chloroquine, 100  $\mu$ M, 3 h).
- (J and L) Bars represent mean values  $\pm$  SEM.

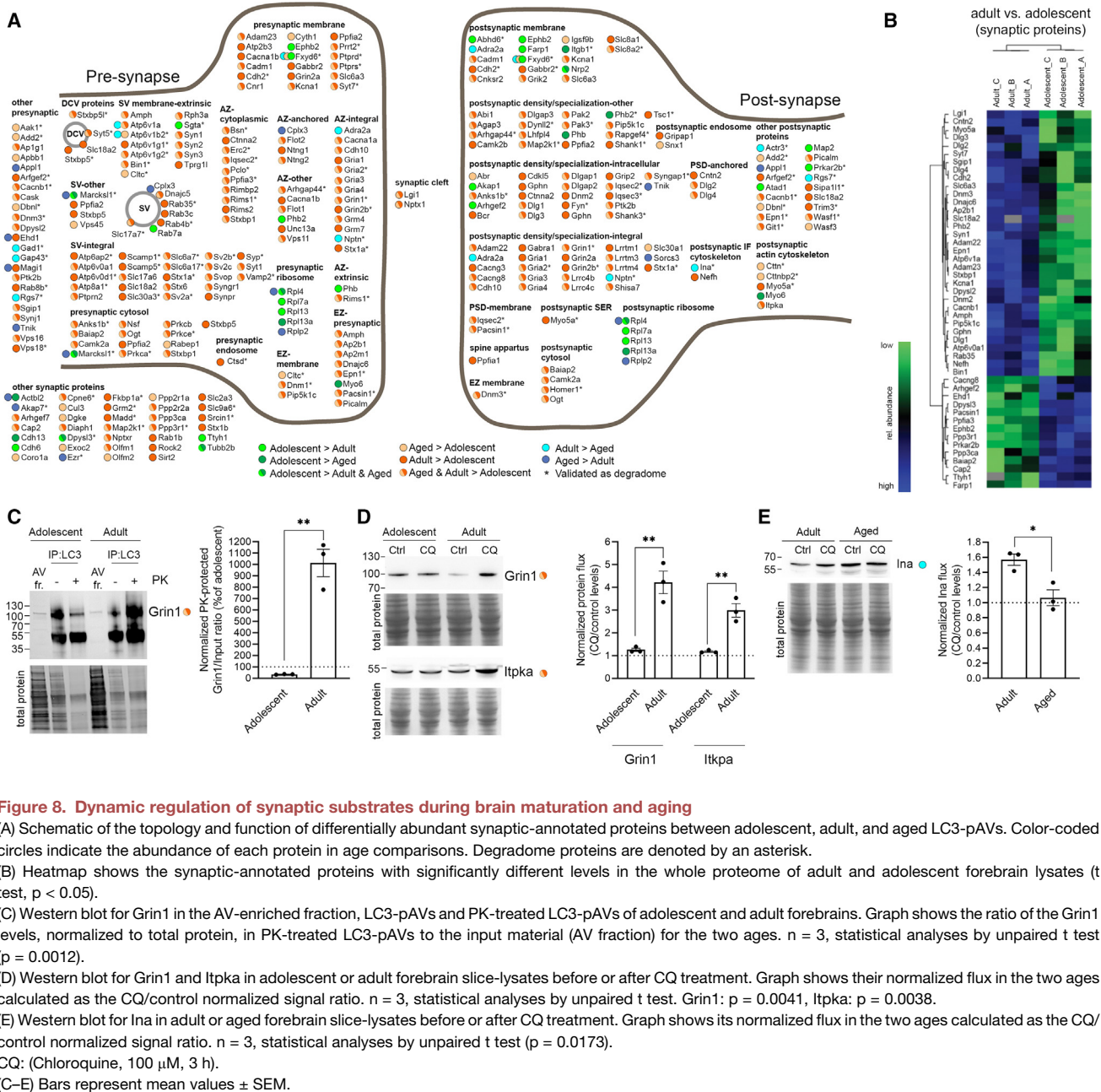


**Figure 8. Dynamic regulation of synaptic substrates during brain maturation and aging**  
 (A) Schematic of the topology and function of differentially abundant synaptic-annotated proteins between adolescent, adult, and aged LC3-pAVs. Color-coded circles indicate the abundance of each protein in age comparisons. Degradome proteins are denoted by an asterisk.  
 (B) Heatmap shows the synaptic-annotated proteins with significantly different levels in the whole proteome of adult and adolescent forebrain lysates (t test,  $p < 0.05$ ).  
 (C) Western blot for Grin1 in the AV-enriched fraction, LC3-pAVs and PK-treated LC3-pAVs of adolescent and adult forebrains. Graph shows the ratio of the Grin1 levels, normalized to total protein, in PK-treated LC3-pAVs to the input material (AV fraction) for the two ages.  $n = 3$ , statistical analyses by unpaired t test ( $p = 0.0012$ ).  
 (D) Western blot for Grin1 and Itpka in adolescent or adult forebrain slice-lysates before or after CQ treatment. Graph shows their normalized flux in the two ages calculated as the CQ/control normalized signal ratio.  $n = 3$ , statistical analyses by unpaired t test. Grin1:  $p = 0.0041$ , Itpka:  $p = 0.0038$ .  
 (E) Western blot for Ina in adult or aged forebrain slice-lysates before or after CQ treatment. Graph shows its normalized flux in the two ages calculated as the CQ/control normalized signal ratio.  $n = 3$ , statistical analyses by unpaired t test ( $p = 0.0173$ ).  
 CQ: (Chloroquine, 100  $\mu$ M, 3 h).  
 (C–E) Bars represent mean values  $\pm$  SEM.

these are validated as degradomes. It is worth-noting that only 50 of the 273 synaptic degradome proteins accumulated in the *nestin-cKO* paradigm, and instead most accumulated in paradigms where lysosomal acidification was impaired. Therefore, in addition to macroautophagy, synaptic proteins may follow alternative routes to the lysosome to safeguard their proteostasis. Another explanation may be that *nestin-cKO*s were analyzed at adolescence due to the progressive neurodegeneration they exhibit. As discussed below, autophagic turnover of synaptic proteins is less prominent in the adolescent brain, making it a nonideal age for revealing differences in the synaptic degradome. The synaptic degradome includes prominent players of

neurotransmission and synaptic plasticity, whose proteostatic deregulation could contribute to the impaired synaptic function observed in autophagy-deficient mouse models<sup>8,9,11,12,14,16,57</sup> or to autophagy-related synaptopathies in humans.<sup>5</sup>

The synaptic LC3-pAV content not validated as degradome likely reflects compensatory mechanisms that safeguard a basal synaptic fitness even after chronic autophagy deficiency. Consistently, some of these synaptic substrates were also reported as proteasomal substrates.<sup>58</sup> Conversely, as synaptic proteins have long half-lives, they may fail to accumulate in acute paradigms, despite being degraded in the lysosome. Alternatively, a population of brain AVs may participate in trafficking and secretion, as

was previously shown for other cell types.<sup>59</sup> However, brain autophagy has thus far been regarded in the context of degradation, with the exception of a few diseases implicating it in the secretion of pathological proteins.<sup>60,61</sup>

Comparative analysis of the LC3-pAV degradome across ages revealed the dynamic nature of autophagic substrates, with synaptic proteins progressively enriched in the adult and aged LC3-pAVs and mitochondrial substrates in the young LC3-pAVs. Notably, no major differences were observed between the adult and aged brains, despite the prevailing view that brain autophagy declines with aging. However, this view has been led by studies in invertebrate models, where the evidence is accompanied by measurable effects on organismal lifespan.<sup>62</sup> Yet, in mammals, there are contradictory findings on whether brain autophagy declines with normal aging.<sup>63</sup> As invertebrates and mammals are subject to different evolutionary forces, autophagy may decline in the mammalian brain in a non-progressive but acute manner at very advanced aging stages.

In conclusion, our extensive analyses provide a temporally resolved reference map of brain autophagic protein substrates. As these substrates have key functions in regulating metabolic, synaptic, and homeostatic states, our findings will complement and consolidate new and emerging roles of autophagy in brain health and disease.

## STAR★METHODS

Detailed methods are provided in the online version of this paper and include the following:

- **KEY RESOURCES TABLE**
- **RESOURCE AVAILABILITY**
  - Lead contact
  - Materials availability
  - Data and code availability
- **EXPERIMENTAL MODEL AND STUDY PARTICIPANT DETAILS**
  - Animals
  - Primary cultures
- **METHOD DETAILS**
  - Purification of brain LC3-positive AVs
  - Protease K protection assay
  - Electron microscopy
  - Mass spectrometry analysis
  - *Ex vivo* autophagic flux assay
  - Preparation of whole forebrain lysates
  - Western blot analysis
  - Treatment of cell cultures with autophagy inhibitors
  - Transfection of primary cell cultures
  - Immunocytochemistry of primary cultures
  - Confocal imaging
  - Analysis of confocal imaging
  - Bioinformatic analysis
- **QUANTIFICATION AND STATISTICAL ANALYSIS**

### Data availability statement

The mass-spectrometry proteomics data are deposited to the ProteomeXchange Consortium via the PRIDE partner repository with the data-

set identifiers PXD034590 and PXD041376. Project Names: “Profiling of purified autophagic vesicle content and degradome in the maturing and aging brain” and “Profiling of purified autophagic vesicle content and degradome in the maturing and aging brain – Part II.”

## SUPPLEMENTAL INFORMATION

Supplemental information can be found online at <https://doi.org/10.1016/j.neuron.2023.05.011>.

## ACKNOWLEDGMENTS

We thank Dr. Erin Wosnitzka for reading the manuscript and sharing resources, Dr. Irina Kolotueva for electron microscopy support, Dr. Niki Ktena and Prof. Domna Karagozeos for *nestin-cKO* colonies, and Michael Stumpe and Dieter Kressler for mass-spectrometry support.

This work was supported by an ERC grant (714983) to V.N., by the Canton and the University of Fribourg as part of the SKINTEGRITY.CH collaborative research project (J.D.), and a Swiss National Science Foundation grant (310030\_212187, J.D.).

## AUTHOR CONTRIBUTIONS

E.K. performed biochemical experiments; experiments with neurons, astrocytes oligodendrocytes, and forebrain cultures; bioinformatic analyses; illustrations; analyzed data; and contributed to the writing. D.S.S. performed mass-spectrometry experiments, bioinformatic data analyses, illustrations, and contributed to the writing. A.M. and R.C.P. designed, performed, and analyzed experiments with cultured microglia. A.K. performed bioinformatic analyses and illustrations. J.D. and V.N. led the study and contributed to writing the manuscript.

## DECLARATION OF INTERESTS

The authors declare no competing interests.

## INCLUSION AND DIVERSITY

We support inclusive, diverse, and equitable conduct of research.

Received: September 8, 2022

Revised: March 19, 2023

Accepted: May 11, 2023

Published: June 5, 2023

## REFERENCES

1. Mizushima, N., and Komatsu, M. (2011). Autophagy: renovation of cells and tissues. *Cell* 147, 728–741. <https://doi.org/10.1016/j.cell.2011.10.026>.
2. Mizushima, N. (2011). Autophagy in protein and organelle turnover. *Cold Spring Harb. Symp. Quant. Biol.* 76, 397–402. <https://doi.org/10.1101/sqb.2011.76.011023>.
3. Itakura, E., Kishi-Itakura, C., and Mizushima, N. (2012). The hairpin-type tail-anchored SNARE syntaxin 17 targets to autophagosomes for fusion with endosomes/lysosomes. *Cell* 151, 1256–1269. <https://doi.org/10.1016/j.cell.2012.11.001>.
4. Lamark, T., and Johansen, T. (2021). Mechanisms of selective autophagy. *Annu. Rev. Cell Dev. Biol.* 37, 143–169. <https://doi.org/10.1146/annurev-cellbio-120219-035530>.
5. Ebrahimi-Fakhari, D., Saffari, A., Wahlster, L., Lu, J., Byrne, S., Hoffmann, G.F., Jungbluth, H., and Sahin, M. (2016). Congenital disorders of autophagy: an emerging novel class of inborn errors of neuro-metabolism. *Brain* 139, 317–337. <https://doi.org/10.1093/brain/awv371>.
6. Glatigny, M., Moriceau, S., Rivagorda, M., Ramos-Brossier, M., Nascimbeni, A.C., Lante, F., Shanley, M.R., Boudarene, N., Rousseaud, A., Friedman, A.K., et al. (2019). Autophagy is required for memory

- formation and reverses age-related memory decline. *Curr Biol* 29, 435–448 e438. <https://doi.org/10.1016/j.cub.2018.12.021>.
7. Pandey, K., Yu, X.W., Steinmetz, A., and Alberini, C.M. (2021). Autophagy coupled to translation is required for long-term memory. *Autophagy* 17, 1614–1635. <https://doi.org/10.1080/15548627.2020.1775393>.
  8. Tang, G., Gudsnuk, K., Kuo, S.H., Cotrina, M.L., Rosoklija, G., Sosunov, A., Sonders, M.S., Kanter, E., Castagna, C., Yamamoto, A., et al. (2014). Loss of mTOR-dependent macroautophagy causes autistic-like synaptic pruning deficits. *Neuron* 83, 1131–1143. <https://doi.org/10.1016/j.neuron.2014.07.040>.
  9. Compans, B., Camus, C., Kallergi, E., Sposini, S., Martineau, M., Butler, C., Kechkar, A., Klaassen, R.V., Retailleau, N., Sejnowski, T.J., et al. (2021). NMDAR-dependent long-term depression is associated with increased short term plasticity through autophagy mediated loss of PSD-95. *Nat. Commun.* 12, 2849. <https://doi.org/10.1038/s41467-021-23133-9>.
  10. Hara, T., Nakamura, M., Matsui, M., Yamamoto, A., Nakahara, Y., Suzuki-Migishima, R., Yokoyama, M., Mishima, K., Saito, I., Okano, H., and Mizushima, N. (2006). Suppression of basal autophagy in neural cells causes neurodegenerative disease in mice. *Nature* 441, 885–889. <https://doi.org/10.1038/nature04724>.
  11. Hernandez, D., Torres, C.A., Setlik, W., Cebrián, C., Mosharov, E.V., Tang, G., Cheng, H.C., Kholidilov, N., Yarygina, O., Burke, R.E., et al. (2012). Regulation of presynaptic neurotransmission by macroautophagy. *Neuron* 74, 277–284. <https://doi.org/10.1016/j.neuron.2012.02.020>.
  12. Kallergi, E., Daskalaki, A.D., Kolaxi, A., Camus, C., Ioannou, E., Mercaldo, V., Haberkant, P., Stein, F., Sidropoulou, K., Dalezios, Y., et al. (2022). Dendritic autophagy degrades postsynaptic proteins and is required for long-term synaptic depression in mice. *Nat. Commun.* 13, 680. <https://doi.org/10.1038/s41467-022-28301-z>.
  13. Komatsu, M., Waguri, S., Chiba, T., Murata, S., Iwata, J., Tanida, I., Ueno, T., Koike, M., Uchiyama, Y., Kominami, E., and Tanaka, K. (2006). Loss of autophagy in the central nervous system causes neurodegeneration in mice. *Nature* 441, 880–884. <https://doi.org/10.1038/nature04723>.
  14. Kuijpers, M., Kochlamazashvili, G., Stumpf, A., Puchkov, D., Swaminathan, A., Lucht, M.T., Krause, E., Maritzen, T., Schmitz, D., and Haucke, V. (2021). Neuronal autophagy regulates presynaptic neurotransmission by controlling the axonal endoplasmic reticulum. *Neuron* 109, 299–313.e9. <https://doi.org/10.1016/j.neuron.2020.10.005>.
  15. Nikolettoulou, V., Sidropoulou, K., Kallergi, E., Dalezios, Y., and Tavernarakis, N. (2017). Modulation of autophagy by BDNF underlies synaptic plasticity. *Cell Metab.* 26, 230–242.e5. <https://doi.org/10.1016/j.cmet.2017.06.005>.
  16. Pan, Y., He, X., Li, C., Li, Y., Li, W., Zhang, H., Wang, Y., Zhou, G., Yang, J., Li, J., et al. (2021). Neuronal activity recruits the CRTCL1/CREB axis to drive transcription-dependent autophagy for maintaining late-phase LTD. *Cell Rep.* 36, 109398. <https://doi.org/10.1016/j.celrep.2021.109398>.
  17. Le Guerroué, F., Eck, F., Jung, J., Starzetz, T., Mittelbronn, M., Kaulich, M., and Behrends, C. (2017). Autophagosomal content profiling reveals an LC3C-dependent piecemeal mitophagy pathway. *Mol. Cell* 68, 786–796.e6. <https://doi.org/10.1016/j.molcel.2017.10.029>.
  18. Zellner, S., and Behrends, C. (2021). Autophagosomal content profiling reveals receptor-specific cargo candidates. *Autophagy* 17, 1281–1283. <https://doi.org/10.1080/15548627.2021.1909410>.
  19. Zellner, S., Schifferer, M., and Behrends, C. (2021). Systematically defining selective autophagy receptor-specific cargo using autophagosomal content profiling. *Mol. Cell* 81, 1337–1354.e8. <https://doi.org/10.1016/j.molcel.2021.01.009>.
  20. Dengjel, J., Hoyer-Hansen, M., Nielsen, M.O., Eisenberg, T., Harder, L.M., Schandorff, S., Farkas, T., Kirkegaard, T., Becker, A.C., Schroeder, S., et al. (2012). Identification of autophagosomal-associated proteins and regulators by quantitative proteomic analysis and genetic screens. *Mol. Cell. Proteomics* 11, M111.014035. <https://doi.org/10.1074/mcp.M111.014035>.
  21. Mancias, J.D., Wang, X., Gygi, S.P., Harper, J.W., and Kimmelman, A.C. (2014). Quantitative proteomics identifies NCOA4 as the cargo receptor mediating ferritinophagy. *Nature* 509, 105–109. <https://doi.org/10.1038/nature13148>.
  22. Øverbye, A., Fengsrud, M., and Seglen, P.O. (2007). Proteomic analysis of membrane-associated proteins from rat liver autophagosomes. *Autophagy* 3, 300–322. <https://doi.org/10.4161/auto.3910>.
  23. Heckmann, B.L., Boada-Romero, E., Cunha, L.D., Magne, J., and Green, D.R. (2017). LC3-associated phagocytosis and inflammation. *J. Mol. Biol.* 429, 3561–3576. <https://doi.org/10.1016/j.jmb.2017.08.012>.
  24. Heckmann, B.L., and Green, D.R. (2019). LC3-associated phagocytosis at a glance. *J. Cell Sci.* 132. <https://doi.org/10.1242/jcs.222984>.
  25. Martinez, J., Malireddi, R.K., Lu, Q., Cunha, L.D., Pelletier, S., Gingras, S., Orchard, R., Guan, J.L., Tan, H., Peng, J., et al. (2015). Molecular characterization of LC3-associated phagocytosis reveals distinct roles for Rubicon, NOX2 and autophagy proteins. *Nat. Cell Biol.* 17, 893–906. <https://doi.org/10.1038/ncb3192>.
  26. Florey, O., Gammoh, N., Kim, S.E., Jiang, X., and Overholtzer, M. (2015). V-ATPase and osmotic imbalances activate endolysosomal LC3 lipidation. *Autophagy* 11, 88–99. <https://doi.org/10.4161/15548627.2014.984277>.
  27. Jacquin, E., Leclerc-Mercier, S., Judon, C., Blanchard, E., Fraitag, S., and Florey, O. (2017). Pharmacological modulators of autophagy activate a parallel noncanonical pathway driving unconventional LC3 lipidation. *Autophagy* 13, 854–867. <https://doi.org/10.1080/15548627.2017.1287653>.
  28. Goldsmith, J., Ordureau, A., Harper, J.W., and Holzbaur, E.L.F. (2022). Brain-derived autophagosome profiling reveals the engulfment of nucleoid-enriched mitochondrial fragments by basal autophagy in neurons. *Neuron* 110, 967–976.e8. <https://doi.org/10.1016/j.neuron.2021.12.029>.
  29. Peña-Martinez, C., Rickman, A.D., and Heckmann, B.L. (2022). Beyond autophagy: LC3-associated phagocytosis and endocytosis. *Sci. Adv.* 8, eabn1702. <https://doi.org/10.1126/sciadv.abn1702>.
  30. Durgan, J., and Florey, O. (2022). Many roads lead to CASM: diverse stimuli of noncanonical autophagy share a unifying molecular mechanism. *Sci. Adv.* 8, eabo1274. <https://doi.org/10.1126/sciadv.abo1274>.
  31. Lin, F., Wang, Z.V., and Hill, J.A. (2014). Seeing is believing: dynamic changes in renal epithelial autophagy during injury and repair. *Autophagy* 10, 691–693. <https://doi.org/10.4161/auto.27749>.
  32. Sharma, K., Schmitt, S., Bergner, C.G., Tyanova, S., Kannaiyan, N., Manrique-Hoyos, N., Kongi, K., Cantuti, L., Hanisch, U.K., Philips, M.A., et al. (2015). Cell type- and brain region-resolved mouse brain proteome. *Nat. Neurosci.* 18, 1819–1831. <https://doi.org/10.1038/nn.4160>.
  33. Rath, S., Sharma, R., Gupta, R., Ast, T., Chan, C., Durham, T.J., Goodman, R.P., Grabarek, Z., Haas, M.E., Hung, W.H.W., et al. (2021). MitoCarta3.0: an updated mitochondrial proteome now with sub-organelle localization and pathway annotations. *Nucleic Acids Res.* 49, D1541–D1547. <https://doi.org/10.1093/nar/gkaa1011>.
  34. Thul, P.J., Åkesson, L., Wiking, M., Mahdessian, D., Geladaki, A., Ait Blal, H., Alm, T., Asplund, A., Björk, L., Breckels, L.M., et al. (2017). A subcellular map of the human proteome. *Science* 356. <https://doi.org/10.1126/science.aal3321>.
  35. Reggio, A., Buonomo, V., Berkane, R., Bhaskara, R.M., Tellechea, M., Peluso, I., Polishchuk, E., Di Lorenzo, G., Cirillo, C., Esposito, M., et al. (2021). Role of FAM134 paralogues in endoplasmic reticulum remodeling, ER-phagy, and Collagen quality control. *EMBO Rep.* 22, e52289. <https://doi.org/10.15252/embr.202052289>.
  36. Noda, N.N., Ohsumi, Y., and Inagaki, F. (2010). Atg8-family interacting motif crucial for selective autophagy. *FEBS Lett.* 584, 1379–1385. <https://doi.org/10.1016/j.febslet.2010.01.018>.
  37. Popelka, H., and Klionsky, D.J. (2015). Analysis of the native conformation of the LIR/AIM motif in the Atg8/LC3/GABARAP-binding proteins. *Autophagy* 11, 2153–2159. <https://doi.org/10.1080/15548627.2015.1111503>.
  38. Kalvari, I., Tsompanis, S., Mulakkal, N.C., Osgood, R., Johansen, T., Nezis, I.P., and Promponas, V.J. (2014). iLIR: a web resource for prediction of Atg8-family interacting proteins. *Autophagy* 10, 913–925. <https://doi.org/10.4161/auto.28260>.

39. Jacomin, A.C., Samavedam, S., Charles, H., and Nezis, I.P. (2017). iLIR@viral: a web resource for LIR motif-containing proteins in viruses. *Autophagy* *13*, 1782–1789. <https://doi.org/10.1080/15548627.2017.1356978>.
40. Heckmann, B.L., Teubner, B.J.W., Tummers, B., Boada-Romero, E., Harris, L., Yang, M., Guy, C.S., Zakharenko, S.S., and Green, D.R. (2020). LC3-associated endocytosis facilitates beta-amyloid clearance and mitigates neurodegeneration in murine Alzheimer's disease. *Cell* *183*, 1733–1734. <https://doi.org/10.1016/j.cell.2020.11.033>.
41. Lucin, K.M., O'Brien, C.E., Bieri, G., Czirr, E., Mosher, K.I., Abbey, R.J., Mastroeni, D.F., Rogers, J., Spencer, B., Masliah, E., and Wyss-Coray, T. (2013). Microglial beclin 1 regulates retromer trafficking and phagocytosis and is impaired in Alzheimer's disease. *Neuron* *79*, 873–886. <https://doi.org/10.1016/j.neuron.2013.06.046>.
42. Jülg, J., Strohm, L., and Behrends, C. (2021). Canonical and noncanonical autophagy pathways in microglia. *Mol. Cell. Biol.* *41*, e0038920. <https://doi.org/10.1128/MCB.00389-20>.
43. Magné, J., and Green, D.R. (2022). LC3-associated endocytosis and the functions of Rubicon and ATG16L1. *Sci. Adv.* *8*, eabo5600. <https://doi.org/10.1126/sciadv.abo5600>.
44. Beese, C.J., Brynjólfssdóttir, S.H., and Frankel, L.B. (2019). Selective autophagy of the protein homeostasis machinery: ribophagy, Proteaphagy and ER-phagy. *Front. Cell Dev. Biol.* *7*, 373. <https://doi.org/10.3389/fcell.2019.00373>.
45. Behrendt, L., Hoischen, C., and Kaether, C. (2021). Disease-causing mutated ATLASTIN 3 is excluded from distal axons and reduces axonal autophagy. *Neurobiol. Dis.* *155*, 105400. <https://doi.org/10.1016/j.nbd.2021.105400>.
46. Dragich, J.M., Kuwajima, T., Hirose-Ikeda, M., Yoon, M.S., Eenjes, E., Bosco, J.R., Fox, L.M., Lystad, A.H., Oo, T.F., Yarygina, O., et al. (2016). Autophagy linked FYVE (Alfy/WDFY3) is required for establishing neuronal connectivity in the mammalian brain. *Elife* *5*, e14810. <https://doi.org/10.7554/eLife.14810>.
47. Sarraf, S.A., Shah, H.V., Kanfer, G., Pickrell, A.M., Holtzclaw, L.A., Ward, M.E., and Youle, R.J. (2020). Loss of TAX1BP1-directed autophagy results in protein aggregate accumulation in the brain. *Mol. Cell* *80*, 779–795.e10. <https://doi.org/10.1016/j.molcel.2020.10.041>.
48. Stavoe, A.K., Gopal, P.P., Gubas, A., Tooze, S.A., and Holzbaur, E.L. (2019). Expression of WIPI2B counteracts age-related decline in autophagosome biogenesis in neurons. *Elife* *8*, e44219. <https://doi.org/10.7554/eLife.44219>.
49. McWilliams, T.G., Prescott, A.R., Montava-Garriga, L., Ball, G., Singh, F., Barini, E., Muqit, M.M.K., Brooks, S.P., and Ganley, I.G. (2018). Basal mitophagy occurs independently of PINK1 in mouse tissues of high metabolic demand. *Cell Metab.* *27*, 439–449.e5. <https://doi.org/10.1016/j.cmet.2017.12.008>.
50. Ordureau, A., Kraus, F., Zhang, J., An, H., Park, S., Ahfeldt, T., Paulo, J.A., and Harper, J.W. (2021). Temporal proteomics during neurogenesis reveals large-scale proteome and organelle remodeling via selective autophagy. *Mol. Cell* *81*, 5082–5098.e11. <https://doi.org/10.1016/j.molcel.2021.10.001>.
51. Lou, G., Palikaras, K., Lautrup, S., Scheibye-Knudsen, M., Tavernarakis, N., and Fang, E.F. (2020). Mitophagy and neuroprotection. *Trends Mol. Med.* *26*, 8–20. <https://doi.org/10.1016/j.molmed.2019.07.002>.
52. Chino, H., and Mizushima, N. (2020). ER-phagy: quality control and turnover of endoplasmic reticulum. *Trends Cell Biol.* *30*, 384–398. <https://doi.org/10.1016/j.tcb.2020.02.001>.
53. Nthiga, T.M., Shrestha, B.K., Bruun, J.A., Larsen, K.B., Lamark, T., and Johansen, T. (2021). Regulation of Golgi turnover by CALCOCO1-mediated selective autophagy. *J. Cell Biol.* *220*, e202006128. <https://doi.org/10.1083/jcb.202006128>.
54. Nthiga, T.M., Shrestha, B.K., Lamark, T., and Johansen, T. (2020). CALCOCO1 is a soluble reticulophagy receptor. *Autophagy* *16*, 1729–1731. <https://doi.org/10.1080/15548627.2020.1797289>.
55. Bhaskara, R.M., Grumati, P., Garcia-Pardo, J., Kalayil, S., Covarrubias-Pinto, A., Chen, W., Kudryashev, M., Dikic, I., and Hummer, G. (2019). Curvature induction and membrane remodeling by FAM134B reticulon homology domain assist selective ER-phagy. *Nat. Commun.* *10*, 2370. <https://doi.org/10.1038/s41467-019-10345-3>.
56. Kurth, I., Pamminger, T., Hennings, J.C., Soehendra, D., Huebner, A.K., Rotthier, A., Baets, J., Senderek, J., Topaloglu, H., Farrell, S.A., et al. (2009). Mutations in FAM134B, encoding a newly identified Golgi protein, cause severe sensory and autonomic neuropathy. *Nat. Genet.* *41*, 1179–1181. <https://doi.org/10.1038/ng.464>.
57. Daskalaki, A.D., Kallergi, E., Kolaxi, A., and Nikolettou, V. (2022). Local biogenesis of autophagic vesicles in neuronal dendrites facilitates long-term synaptic depression. *Autophagy* *18*, 2011–2012. <https://doi.org/10.1080/15548627.2022.2061757>.
58. Bingol, B., and Schuman, E.M. (2005). Synaptic protein degradation by the ubiquitin proteasome system. *Curr. Opin. Neurobiol.* *15*, 536–541. <https://doi.org/10.1016/j.conb.2005.08.016>.
59. Jiang, S., Dupont, N., Castillo, E.F., and Deretic, V. (2013). Secretory versus degradative autophagy: unconventional secretion of inflammatory mediators. *J. Innate Immun.* *5*, 471–479. <https://doi.org/10.1159/000346707>.
60. Lim, J., and Yue, Z. (2015). Neuronal aggregates: formation, clearance, and spreading. *Dev. Cell* *32*, 491–501. <https://doi.org/10.1016/j.devcel.2015.02.002>.
61. Nilsson, P., Loganathan, K., Sekiguchi, M., Matsuba, Y., Hui, K., Tsubuki, S., Tanaka, M., Iwata, N., Saito, T., and Saido, T.C. (2013). Abeta secretion and plaque formation depend on autophagy. *Cell Rep.* *5*, 61–69. <https://doi.org/10.1016/j.celrep.2013.08.042>.
62. Aman, Y., Schmauck-Medina, T., Hansen, M., Morimoto, R.I., Simon, A.K., Bjedov, I., Palikaras, K., Simonsen, A., Johansen, T., Tavernarakis, N., et al. (2021). Autophagy in healthy aging and disease. *Nat Aging* *1*, 634–650. <https://doi.org/10.1038/s43587-021-00098-4>.
63. Kallergi, E., and Nikolettou, V. (2021). Macroautophagy and normal aging of the nervous system: lessons from animal models. *Cell Stress* *5*, 146–166. <https://doi.org/10.15698/cst2021.10.257>.
64. Hu, Z., Sankar, D.S., Vu, B., Leytens, A., Vionnet, C., Wu, W., Stumpe, M., Martínez-Martínez, E., Stork, B., and Dengjel, J. (2021). ULK1 phosphorylation of striatin activates protein phosphatase 2A and autophagy. *Cell Rep.* *36*, 109762. <https://doi.org/10.1016/j.celrep.2021.109762>.
65. Cox, J., and Mann, M. (2008). MaxQuant enables high peptide identification rates, individualized p.p.b.-range mass accuracies and proteome-wide protein quantification. *Nat. Biotechnol.* *26*, 1367–1372. <https://doi.org/10.1038/nbt.1511>.
66. Tyanova, S., Temu, T., Sinitcyn, P., Carlson, A., Hein, M.Y., Geiger, T., Mann, M., and Cox, J. (2016). The Perseus computational platform for comprehensive analysis of (prote)omics data. *Nat. Methods* *13*, 731–740. <https://doi.org/10.1038/nmeth.3901>.
67. Shen, H., Zhu, H., Panja, D., Gu, Q., and Li, Z. (2020). Autophagy controls the induction and developmental decline of NMDAR-LTD through endocytic recycling. *Nat. Commun.* *11*, 2979. <https://doi.org/10.1038/s41467-020-16794-5>.

## STAR★METHODS

### KEY RESOURCES TABLE

REAGENT or RESOURCE	SOURCE	IDENTIFIER
<b>Antibodies</b>		
anti-LC3A	Genetex	Cat# GTX17380
anti-LC3B rabbit	Sigma-Aldrich	Cat# L7543
anti-Atf3	Proteintech	Cat# 16921-1-AP
anti-Atg5	Novus Biologicals	Cat# NBP2-24389
anti-Atg9a (SC67-05)	Novus Biologicals	Cat# NBP2-67616
anti-Atg13	Sigma-Aldrich	Cat# SAB4200100
anti-Alfy/Wdfy3	Santa Cruz	Cat# sc-514569
anti-Bassoon	Abcam	Cat# ab82958
anti-Bcl2l13	Proteintech	Cat# 16612-1-AP
anti-Bnip3l	Abcam	Cat# ab109362
anti-Calr	Proteintech	Cat# 27298-1-AP
anti-Dynamin1	Abcam	Cat# ab52611
anti-Fam134a	Novus Biologicals	Cat# NBP2-76380
anti-Fkbp8	Atlas Antibodies	Cat# HPA045177
anti-Fundc1	Abcam	Cat# ab224722
anti-GABARAPL1 (D5R9Y)	Cell Signaling	Cat# 26632S
anti-GFAP	Sigma-Aldrich	Cat# G3893
anti-GFP	Invitrogen	Cat# A-11122
anti-Gria2	Synaptic Systems	Cat# 182211
anti-Grin1	Invitrogen	Cat# PA3-102
anti-Grin2b	Alomone	Cat# AGC-003
anti-alpha internexin (2E3) (Ina)	Invitrogen	Cat# 32-3600
anti-K63 ubiquitin	Merck	Cat# 05-1308
anti-IgG	Milipore	Cat# 12-370
anti-MAP2	Synaptic Systems	Cat# 188004
anti-Neurofilament H	Synaptic Systems	Cat# 171104
anti-Neurofilament H	Abcam	Cat# ab7794
anti-Nipsnap1	Novus Biologicals	Cat# NBP1-76888
anti-oligodendrocyte marker O4	Sigma-Aldrich	Cat# O7139
anti-p62/sqstm1	Abcam	Cat# ab56416
anti-p62/sqstm1	Progen	Cat# GP62-C
anti-pAtg13	Rockland	Cat# 600-401-C49
anti-Phb2	Proteintech	Cat# 12295-1-AP
anti-P2Y12R	Biologend	Cat# 848002
anti-Rab1b	Proteintech	Cat# 17824-1-AP
anti-Rims1	Bethyl Laboratories	Cat# A305-040A-T
anti-Rab7	Abcam	Cat# ab137029
anti-Rtn3/HAP	Abcam	Cat# ab187764
anti-Rtn4/NOGO	Proteintech	Cat# 10740-1-AP
anti-Sacm1/Sac1	Proteintech	Cat# 13033-1-AP
anti-Shank3	Abcam	Cat# ab93607
anti-Syt7 (synaptotagmin 7)	Abcam	Cat# ab106618
anti-Tax1bp1	Proteintech	Cat# 14424-1-AP

(Continued on next page)

**Continued**

REAGENT or RESOURCE	SOURCE	IDENTIFIER
anti-Tecr	Bethyl Laboratories	Cat# A305-515A
anti-Tollip	Abcam	Cat# ab223763
anti-Ubiquitin	Invitrogen	Cat# 14-6078-82
anti-Vapa	Proteintech	Cat# 15275-1-AP
anti-Wipi2	Abcam	Cat# ab105459
anti-rabbit IgG (H+L)	Jackson	Cat# 211-035-109
anti-mouse IgG (H+L)	Jackson	Cat# 715-035-150
anti-mouse IgG (Dylight 800 4xPEG)	Invitrogen	Cat# SA5-35521
anti-Mouse IgG H&L (Alexa Fluor Plus) 647	Thermo Fisher Scientific	Cat# A32787
anti-Rabbit IgG H&L (Alexa Fluor Plus) 555	Thermo Fisher Scientific	Cat# A32794
Goat anti-Rabbit IgG H&L (Alexa Fluor) 488	Abcam	Cat# ab150077
Goat anti-Guinea pig IgG H&L (Alexa Fluor) 647	Abcam	Cat# ab150187
Goat anti-Mouse IgG H&L (Alexa Fluor) 594	Abcam	Cat# ab150116
Donkey anti-Rat IgG H&L (Alexa Fluor 488)	Thermo Fisher Scientific	Cat# A21208
<b>Chemicals, plasmids, peptides, and recombinant proteins</b>		
Amphotericin B	PAN-Biotech	Cat# P06-01100
Bafilomycin A1	Sigma-Aldrich	Cat# B1793
B27™ Plus Supplement	Life Technologies Europe BV	Cat# A35828-01
Bovine serum albumin (BSA)	VWR	Cat# 9048-46-8
Bovine serum albumin (BSA)	Sigma-Aldrich	Cat# A8806
CellLight™ ER-GFP BacMam 2.0	Invitrogen	Cat# C10590
CellLight™ Mito-GFP BacMam 2.0	Invitrogen	Cat# C10600
Chloroquine diphosphate salt (CQ)	Sigma-Aldrich	Cat# C6628
cOmplete™, Mini, EDTA-free Protease Inhibitor Cocktail	Merck	Cat# 11836170001
D-Biotin	Sigma-Aldrich	Cat# B4501
4',6-Diamidino-2-Phenylindole, Dihydrochloride (DAPI)	Thermo Fisher Scientific	Cat# D1306
D-(+)-Glucose	Sigma-Aldrich	Cat# G8769
DPBS (1x)	Gibco	Cat# 14190-144
DMEM advanced 1x	Gibco	Cat# 12491-015
DMEM 4.5 g/L of glucose	Thermo Fisher Scientific	Cat# 41966052
DMEM (1x) + GlutaMAX™-I	Gibco	Cat# 61965-026
Dimethyl sulfoxide (DMSO)	Roth	Cat# A994.1
Dimethyl sulfoxide (DMSO)	Sigma-Aldrich	Cat# D8418
Dynabeads™ Protein G Immunoprecipitation Kit	Life Technologies Europe BV	Cat# 10007D
Fetal Bovine Serum (FBS)	Thermo Fisher Scientific	Cat# 10500-064
Fluoroshield Mounting Medium	Abcam	Cat# ab104135
Formalin solution, neutral buffered, 10%	Sigma-Aldrich	Cat# HT501128
Glycyl-L-Phenylalanine 2-Naphthylamide (GPN)	Abcam	Cat# ab145914
Hoechst 33342 nuclear dye	HelloBio	Cat# HB0787
HBSS (1x)	Gibco	Cat# 24020-091
L-glutamine	Life Technologies Europe BV)	Cat# 25030123
MEM 1x, no glutamine	Gibco	Cat# 21090-022
Mowiol (polyvinyl alcohol) 4-88	Sigma-Aldrich	Ca# 81381
Neurobasal Plus Medium	Gibco	Cat# A35829-01

(Continued on next page)

**Continued**

REAGENT or RESOURCE	SOURCE	IDENTIFIER
N2 supplement	ThermoFisher Scientific	Cat# 17502
N-acetyl-L-cysteine	Sigma-Aldrich	Cat# A8199
Neurobasal Plus medium	Life Technologies Europe BV	Cat# A3653401
Nycodenz	Axon Lab	Cat# 1002424
OptiPrep Density Gradient Medium	Sigma-Aldrich	Cat# D1556
Percoll	GE Healthcare	Cat# 17-0891-01
Penicillin-Streptomycin	Thermo Fisher Scientific	Cat# 15140-122
Penicilin-Streptomycin-Glutamine 100x	Gibco	Cat# 10378016
Paraformaldehyde (PFA)	Sigma Merck	Cat# 16005
Poly-D-Lysine hydrobromide	Sigma Merck	Cat# P6407
Poly-D-Lysine-coated glass coverslip, 5 mm (0.13-0.16 mm)	Thermo Fisher Scientific	Cat# 11888372
Proteinase K	Merck	Cat# P2308
Phenylmethylsulfonyl fluoride (PMSF)	Sigma-Aldrich	Cat# P7626
Phosphatase Inhibitor Cocktail I	Abcam	Cat# ab201112
SAR405	LubioScience	Cat# S7682
SBI-0206965	Sigma-Aldrich	Cat# SML1540
SuperSignal™ West Femto	Life Technologies Europe BV	Cat# 34095
SuperSignal™ West Pico PLUS	Life Technologies Europe BV	Cat# 34580
3,3',5-Triiodo-L-thyronine sodium salt (T3)	Sigma-Aldrich	Cat# T6397
TripLE Express Enzyme Solution	Thermo Fisher Scientific	Cat# 12-604-021
Trypsin-EDTA 0.05% (1x)	Gibco	Cat# 25300-054
<b>Other consumables</b>		
Coverslips diameter 12mm #1 (0.13-0.16mm)	Roth	Cat# P231.1
75cm <sup>2</sup> flasks	VWR	Cat# 734-2314
6-well plates (Nuclon™ Delta surface)	Thermo Scientific	Cat# 140675
24-well plates (Nuclon™ Delta surface)	Thermo Scientific	Cat# 142475

**RESOURCE AVAILABILITY**

**Lead contact**

Further information and requests for resources and reagents should be directed to and will be fulfilled by the Lead Contact, Prof. Vassiliki Nikolettou, email address: Vassiliki.nikolettou@unil.ch

**Materials availability**

This study did not generate new unique reagents.

**Data and code availability**

- The mass spectrometry proteomics data are deposited to the ProteomeXchange Consortium via the PRIDE partner repository with the dataset identifiers PXD034590 and PXD041376. Project Names: “Profiling of purified autophagic vesicle content and degradome in the maturing and aging brain” and “Profiling of purified autophagic vesicle content and degradome in the maturing and aging brain - Part II”.
- This paper does not report original code.
- Any additional information required to reanalyze the data reported in this paper is available from the lead contact upon request.

**EXPERIMENTAL MODEL AND STUDY PARTICIPANT DETAILS**

**Animals**

Animal procedures were approved by the Swiss veterinary services of the Canton Vaud (Direction generale de l'agriculture, de la viticulture et des affaires veterinaires, license number VD3460). The mice were maintained in a pathogen-free environment and housed

in groups of five animals per cage with constant temperature and humidity and a 12h/12h light/dark cycle. The animals used in this study were: wild-type C57BL/6J mice, wild-type CD1 mice and the *CAG-RFP-GFP-LC3* transgenic mice (full strain name: C57BL/6-Tg(CAG-RFP/EGFP/Map11c3b)1Hill/J). Embryos of both sexes, from CD1 or *CAG-RFP-GFP-LC3* mice were used for preparation of primary cultures. C57BL/6J male mice were used at the following ages: Postnatal day 25 (adolescent), 6-month old (adult) and 18-month old (aged).

## Primary cultures

### Neurons

For the preparation of primary neuronal cultures, cortices and hippocampi were isolated from embryos of both sexes, and of embryonic day 14.5 (E14.5), rinsed in ice-cold PBS 1x and centrifuged at 1000g for 5min at room temperature. Cells were dissociated in 0.05% Trypsin-EDTA 1x solution at 37°C for 25min, where tissue was dissociated by pipetting every 10min. After dissociation, the activity of trypsin was quenched by adding equal volume of dissociation medium: “plating medium” (advanced DMEM 1X, 200mM L-glutamine, 1% penicillin/streptomycin and 2% FBS) and FBS in a 1:1 ratio. Cells were then centrifuged at 1000g for 5 min. Neurons were plated in Neurobasal Plus Medium supplemented with 1x B-27™ Plus Supplement, 200mM L-glutamine, 1% penicillin/streptomycin at an initial density of 1.000.000 cells/cm<sup>2</sup> in 6cm plates or 300.000cells/cm<sup>2</sup> in 24-well plates containing PDL-coated glass coverslips. All coverslips were coated for 3h at 37°C with poly-D-lysine 0.05mg/ml. Neurons were cultured for a total of 18 days *in vitro*, with a half medium change every 3–4 days. For the preparation of mixed primary neuronal cultures, the aforementioned procedure was followed, using this time cortices and hippocampi isolated from embryos staged at E17.5–18.5, where gliogenesis has already started. All experiments with primary neurons and mixed forebrain cultures were performed at day *in vitro* 18 (DIV18).

### Astrocytes

Brains from wild-type pups of both sexes at P3–P5 were collected and cerebellum, meninges and olfactory bulbs were eliminated. Both the hemispheres were mechanically smashed with forceps and put into 3ml of TripLE Express Enzyme Solution at 37°C for 20min. The tissue was further dissociated by pipetting with a 1ml tip. Enzymatic reaction was stopped by adding 10ml of culture medium: DMEM 4.5 g/L of glucose, 10% FBS and 1% penicillin-streptomycin. Cells were pelleted at 400g for 4min at RT and the pellet resuspended in fresh culture medium. Cells obtained from each individual brain were seeded into 75cm<sup>2</sup> flasks. After two weeks in culture, microglia were removed for downstream processing, and the remaining astrocytes were washed three times with PBS and cultured in MEM 1x, 10% FBS, 2% penicillin/streptomycin supplemented with glutamine, 1% amphotericin B and 0,3% D-(+)-glucose. Astrocytes were dissociated in 0.025% Trypsin-EDTA 1x diluted in DPBS 1x at 37°C for 10min and trypsin was deactivated. Cells were centrifuged for 7min at 1100g at RT, resuspended in the aforementioned medium and seeded as 20.000cell/cm<sup>2</sup> in 24-well plates containing PDL coated glass coverslips. All coverslips were coated for 3h at 37°C with poly-D-lysine 0.05mg/ml. All experiments were performed 4–5 days after plating in 24-well plates.

### Oligodendrocytes

For the preparation of primary oligodendrocytic cultures, forebrains from postnatal day 1 (P1) CD1 pups of both sexes were isolated, meninges were removed in HBSS 1x and the dissected tissue was trypsinized using trypsin (0.003% in HBSS 1x) for 10min at 37°C. Trypsin was then inactivated by addition of prewarmed mix of HBSS 1x and FBS (5:1). Brain cells were then centrifuged for 5min at 100g, cells were again rinsed with HBSS 1x and FBS (5:1) and the pellet was resuspended in prewarmed “cortex medium”: DMEM (GlutaMAX™ 4.5g/L D-Glucose [-] Pyruvate supplemented with 10% FBS and 1% penicillin/streptomycin. The resuspension in “cortex medium” was repeated 3 times in total, where every time the cells were triturated gently using Pasteur pipette, 1ml and finally 200μl tip. Then, the cells were plated onto poly-D-lysine-coated 75cm<sup>2</sup> culture flasks and the cultures were kept in an incubator with 5% CO<sub>2</sub> at 37°C, up to DIV4, when their medium was completely changed. The culture medium was replenished twice a week, until mixed glial cultures became confluent (after 15 days). At *in vitro* day 15, microglia were removed using an orbital shaker at 200rpm for 1h at 37°C and oligodendrocytic progenitor cell (OPC) population was separated from the underlying layer of astrocytes by vigorous shaking (16h at 240rpm, 37°C). OPCs were then washed and seeded at an initial density of 70,000 cells per well in 24-well plates containing 13mm glass coverslips that had been treated 3h at 37°C with poly-D-lysine. OPCs were then differentiated in mature OLs, by culturing OPCs in “proliferating medium”: DMEM 1x GlutaMAX with 1% N2 supplement, D-biotin 100ng/ml, 0.1% BSA fatty acid-free, N-acetyl-L-cysteine 60μg/ml, 1% penicillin-streptomycin, T3 40ng/ml, PDGF $\alpha$  10ng/ml and hFGF 10ng/ml (this stage is DIV0) for 2 days. Then the medium was changed to “myelinating medium”: DMEM 1x GlutaMAX with 1% N2 supplement, N-acetyl-L-cysteine 60μg/ml, D-biotin 100ng/ml, 1% penicillin-streptomycin, 0.1% BSA fatty acid-free and T3 (40ng/ml). Cells were kept in the aforementioned medium and the treatments with autophagy inhibitors were performed at DIV4.

### Microglia

Brains from wild-type pups of both sexes at P3–P5 were collected and cerebellum, meninges and olfactory bulbs were eliminated. Both the hemispheres were mechanically smashed with forceps and put into 3ml of TripLE Express Enzyme Solution at 37°C for 20min. The tissue was further dissociated by pipetting with a 1ml tip. Enzymatic reaction was stopped by adding 10ml of culture medium: DMEM 4.5 g/L of glucose, 10% FBS and 1% penicillin-streptomycin. Cells were pelleted at 400g for 4min at RT and the pellet resuspended in fresh culture medium. Cells obtained from each individual brain were seeded into 75cm<sup>2</sup>. After two weeks in culture, microglia were harvested by smacking the flask and seeded on a coating of Poly-D-Lysine hydrobromide (0.1 mg/mL, 1h at 37°C). Microglial cells were kept in astrocyte-conditioned medium (ACM) and maintained at 37°C and 5% CO<sub>2</sub>. Microglia were seeded as

10,000 cells/well on Poly-D-Lysine-coated glass coverslips of 5 mm (0.13–0.16 mm). All experiments were performed at DIV5 after seeding.

## METHOD DETAILS

### Purification of brain LC3-positive AVs

#### *Preparation of brain AV-enriched fraction (Step 1)*

Ten forebrains of adult (6-month old) C57BL/6J male mice were used to prepare brain AV-enriched fractions, as previously described.<sup>15</sup> Briefly, the aforementioned brain area was homogenized in 10% sucrose, 10mM HEPES and 1mM EDTA (pH 7.3) by 20 strokes using a Dounce glass homogenizer. The resulting homogenate was sequentially diluted with half volume of homogenization buffer (HB) (250mM sucrose, 10mM HEPES and 1mM EDTA, pH 7.3) containing 1.5mM glycyl-L-phenylalanine 2-naphthylamide (GPN). The resulting material was then incubated at 37°C for 7min, and centrifuged at 2000g for 2min at 4°C. The nuclear pellet was discarded and the post-nuclear supernatant was loaded on discontinuous Nycodenz gradients for centrifugation at 141000g for 1 hour at 4°C, to remove the cytosolic, mitochondrial and peroxisomal fraction. The isolated layer of material, which contained both autophagosomes and endoplasmic reticulum, was further diluted with an equal volume of HB buffer and overlaid on Nycodenz-Percoll gradients. After centrifugation at 72000g for 30min at 4°C to remove the Percoll silica particles, the resulting interface that contained the AVs was diluted with 0.7 volumes of 60% Buffered Optiprep overlaid by 30% Buffered Optiprep and HB buffer. The gradients were then centrifuged at 71000g for 30min at 4°C. The collected AVs were diluted in three volumes of HB buffer and the concentration of the purified isolated AVs was then measured by BCA, following the manufacturer's instructions.

#### *Immuno-purification of brain LC3-positive AVs (Step 2)*

For the immuno-purification experiments, 250µg of the AV-enriched fraction were used as input for the immunoprecipitation with an antibody against LC3B or IgG control. First, 10µg of each antibody was incubated with 50µl Dynabeads™ Protein G magnetic beads for 30min at room temperature (rotating at low speed). Then, the input was added to the Antibody-beads mix for 1h at room temperature (rotating at low speed). Unbound material was centrifuged at 16100g for 30min at 4°C and the pellet was resuspended in Laemmli buffer. Elution was performed following the manufacturer's instructions.

#### *Protease K protection assay*

AV-enriched fraction or purified AVs were washed two times in DPBS 1x and treated with Proteinase K (PK) (20ng/µl) on ice for 20min, in the presence or absence of 1% Triton X-100, and then 4mM of PMSF was added for 10min on ice, for PK inactivation. The samples were then centrifuged at 16100g for 10min at 4°C and the autophagosomal pellets were resuspended in Laemmli buffer, boiled for 5min at 95°C and analyzed by Western blot analysis. To perform the Protease K (PK) protection assay on the LC3-pAVs, 250µg of AV-enriched fraction were used as input for the immunoprecipitation with an antibody against LC3B. After binding of the LC3-pAVs on the Dynabeads™ Protein G magnetic beads (see "*Immuno-purification of brain LC3-positive AVs*" procedure), the manufacturer's protocol was followed up to the step of the washes with DPBS 1x. Then PK digestion of the LC3-pAVs was performed on the beads where PBS 1x supplemented with PK 20ng/µl was directly added to the beads-LC3pAVs for 20min on ice. Elution was performed using Laemmli buffer and by boiling at 95°C for 5min.

#### *Electron microscopy*

Electron microscopy experiments were performed at the EM-facility of the University of Lausanne. PK-treated AV-enriched fractions, the LC3-IP and IgG-IP material bound on the beads, or the unbound material, were pelleted by centrifugation or by using magnetic field and fixed in 2.5% glutaraldehyde; 2% PFA in 0.1M phosphate buffer (PB), pH 7.25 overnight and extensively washed in PB 0.1M. They were then incubated in 2% (wt/vol) osmium tetroxide and 1.5% (wt/vol) K<sub>4</sub>[Fe(CN)<sub>6</sub>] in 100mM PB buffer for 1h on ice. After an extensive wash with water, samples were incubated for 1h in 1% (wt/vol) tannic acid in 100mM PB buffer, followed by 1% (wt/vol) uranyl acetate for 2h at ambient temperature. Finally, samples were dehydrated at ambient temperature in gradual ethanol cycles and infiltrated with a mix of ethanol and Epon-Araldite mix. After several cycles of 100% Epon-Araldite incubations, samples were flat embedded and polymerized for 24h at 60°C. and then embedded in Polymerized flat blocks were trimmed using a 90° diamond trim tool (Diatome, Biel, Switzerland). The arrays of 70nm sections were obtained using a 35° diamond knife (Diatome, Biel, Switzerland) mounted on Leica UC6 microtome (Leica, Vienna). Sections were collected on polyetherimide-coated carbon slot grids. TEM samples were analyzed with an FEI CM100 electron microscope (Thermo Fischer scientific) at 80kV, equipped with a TVIPS camera, piloted by the EMTVIPS program. Images were collected either as single frames or stitched mosaic panels to cover more extensive sample regions. The multiple tile images were stitched with the IMOD software package. Data were processed and analyzed using Fiji, IMOD 3dmod, and Photoshop programs.

#### *Mass spectrometry analysis*

##### *Quantitative MS analyses*

Protein samples (tissue, IPs, cell lysates) were heated in SDS-PAGE loading buffer for 10 minutes at 95°C, treated with 1 mM DTT, and alkylated using 5.5 mM iodoacetamide for 10 minutes at room temperature. Samples were fractionated on 4–12% gradients gels and proteins were in-gel digested with trypsin (Promega), three fractions per sample. Tryptic peptides were purified by

STAGE tips and LC-MS/MS measurements were performed on a QExactive Plus mass spectrometry coupled to an EasyLC 1200 nanoflow-HPLC (all Thermo Scientific) in a data-dependent manner essentially as described.<sup>64</sup> MaxQuant software (version 1.6.2.10)<sup>65</sup> was used for analyzing the MS raw files for peak detection, peptide quantification and identification using a full length Uniprot mouse database (version April 2016). Carbamidomethylcysteine was used as fixed modification and oxidation of methionine as well as N-terminal acetylation were set as variable modifications. The MS/MS tolerance was set to 20 ppm and four missed cleavages were allowed for Trypsin/P as enzyme specificity. Based on a forward-reverse database, protein and peptide FDR were set to 0.01, minimum peptide length was set to seven, and at least one unique peptide had to be identified. The match-between run option was set to 0.7 minutes. MaxQuant results were analysed using Perseus software (version 1.6.2.3).<sup>66</sup>

#### **MS data quantification and statistical analysis**

Label free quantification measurements were obtained for all samples, LFQ values were used for whole proteome analyses. For LC3-pAVs content analysis, iBAQ values of LC3B immunoprecipitation data were normalized to the median of each respective replicate. Missing values in IgG control experiments were imputed using a normal distribution with a width of 0.3 and down shift of 1.8. Missing values in “true” experiments were left blank. A minimum of two out of three valid values per experiment were required for further analyses. Statistical significance was calculated using student T-test with p values <0.05, and FDR corrected p values q<0.05 as shown in respective figures. Perseus software (version 1.6.2.3) was used for all the statistical analysis.

#### **Ex vivo autophagic flux assay**

Coronal forebrain slices (250µm-thick) were prepared using a vibratome, as previously described.<sup>67</sup> Subsequently, brain slices were incubated in oxygenated aCSF for 1h, before their treatments in oxygenated aCSF (124mM NaCl, 3mM KCl, 26mM NaCO<sub>3</sub>, 1.25mM NaH<sub>2</sub>PO<sub>4</sub>, 10mM glucose, 1mM MgSO<sub>4</sub>, 2mM CaCl<sub>2</sub>) supplemented with 120µM chloroquine (CQ) or vehicle for 3hrs at 32° C. After treatment, we prepared forebrain lysates for further western blot analysis.

#### **Preparation of whole forebrain lysates**

Forebrain lysates were prepared from wild-type C57Bl/6J mice of the indicated ages, and from *atg5<sup>fl/fl</sup>* and *nestin-cre;atg5<sup>fl/fl</sup>* mice (kind gift of Prof. Karagozeos lab) as previously described.<sup>15</sup>

#### **Western blot analysis**

Cellular fractions, AV-fractions, LC3-pAVs, cell lysates or forebrain tissue lysates were prepared in 2x Laemmli buffer (20mM Tris-HCl, pH 6.8, 0.2mg/ml bromophenol blue, 4% SDS, 15.6% glycerol containing 3.1% DTT) with the addition of protease and phosphatase inhibitors. Proteins were separated using SDS-PAGE under reducing conditions, transferred to a nitrocellulose membrane and examined by immunoblotting. Briefly, membranes were blocked with shaking in 5% milk in 1x PBS-0,1% Tween 20 for 1h at RT and then in 2% milk in 1x PBS-0,1% Tween 20 with the primary antibodies: Alf1 (1:500), Atf3 (1:1000), Atg5 (1:1000), Atg9a (1:1000), Atg13 (1:1000), Bnip3l (1:1000), Bcl2l13 (1:1000), Gabarapl1 (1:1000), Calu (1:1000), Calr (1:1000), Dynamin 1 (1:1000), Fam134a (1:1000), Fkbp8 (1:1000), Fundc1 (1:1000), Gria2 (1:1000), Grin2b (1:1000), Grin1 (1:1000), Ina (1:1000), Itpk1 (1:1000), K63 ubiquitin (1:1000), LC3A (1:1000), LC3B (1:1000), Nipsnap1 (1:1000), p62 (1:2000), pAtg13 (1:1000), Phb2 (1:1000), Rab7 (1:1000), Rab1b (1:1000), Rims1 (1:1000), Rtn3 (1:1000), Rtn4 (1:1000), Sac1 (1:1000), Shank3 (1:500), Stx17 (1:1000), Syt7 (1:1000), Tax1bp1 (1:1000), Tecr (1:1000), Tollip (1:1000), Ubiquitin (1:1000), Vapa (1:1000) and Wipi2 (1:1000). Then the membranes were washed three times with 1x PBS-Tween 20, for 10min each, and were incubated with appropriate secondary antibodies (1:10000) in 1% milk diluted 1x PBS-0,1% Tween 20 for 1h at RT with shaking. Developing of the membranes was performed using SuperSignal™ West Femto and SuperSignal™ West Pico PLUS. Membranes were scanned using the iBright1500 (Thermo Scientific). Quantification of western blot data was performed using Image J software.

#### **Treatment of cell cultures with autophagy inhibitors**

For the experiments of pharmacological impairment of autophagy in neuronal, astrocytic and oligodendrocytic primary cultures, we used SBI-0206965 (3µM) alone or together with SAR405 (3µM) for a total of 6h, or Bafilomycin A1 (50nM) for a total of 3h. The stages of the cells when treated with the aforementioned drugs were: DIV18 for primary neuronal cultures or mixed primary neuronal cultures, DIV25-26 for the astrocytic cultures and DIV5 for the oligodendrocytic cultures. The different cell populations were then fixed to perform confocal experiments or neuronal cells were lysed in lysis buffer (50mM Tris-HCl, pH 7.4, 150mM NaCl, 1mM EDTA, 1% Triton X-100, 0.1% sodium deoxycholate and 0.1% SDS) to produce lysates for western blot analysis. For all treatments, control neurons, astrocytes or oligodendrocytes were treated with the vehicle at the same concentration (0.1% DMSO) and for the same time duration. For microglial cultures, cells were treated after five days in culture, with DMSO (Roth) or SAR405 (1µM) for 6h.

#### **Transfection of primary cell cultures**

To label the endoplasmic reticulum (ER) or mitochondria of primary neuronal, astrocytic and oligodendrocytic cultures, we used the constructs CellLight™ ER-GFP, BacMam 2.0 and CellLight™ Mitochondria-GFP, BacMam 2.0, respectively. CellLight™ ER-GFP, BacMam 2.0 expresses the green fluorescent protein (GFP) fused to the ER signal sequence of calreticulin and KDEL (ER retention signal) for the case of the ER-labelling, while CellLight™ Mito-GFP, BacMam 2.0 expresses the GFP fused to the leader sequence of E1 alpha pyruvate dehydrogenase for the case of labelling the mitochondria. Briefly, cell cultures were first transfected with the

mentioned constructs for 17h at 37°C, the amount of the reagent was adjusted following the manufacturer's protocol and pharmacological impairment of autophagy was followed as mentioned in the main text.

### Immunocytochemistry of primary cultures

Primary neurons, astrocytes or oligodendrocytes were rinsed in PBS 1x and fixed immediately after with 4% paraformaldehyde (PFA) in PBS 1x for 15min. After fixation, cells were rinsed with DPBS 1x and incubated in blocking solution (10% Fetal Bovine Serum (FBS) and 0.2% Triton X-100 in PBS 1x) for 1h at room temperature (RT). Neurons and astrocytes were then incubated with primary antibodies in blocking buffer (Bassoon 1:1000, Fkbp8 1:500, GFAP 1:1000, GFP 1:1000, K63 Ubiquitin 1:1000, MAP2 1:2000, Neurofilament H 1:1000, O4 1:500, p62 1:1000 and Rtn3 1:1000 (for the transfected cells with BacMam 2.0 constructs)) overnight at 4°C. After three washes with DPBS 1x, cells were incubated with fluorescently labelled secondary antibodies, diluted 1:1000 in DPBS 1x, for 1h at RT together with Hoechst 33342 nuclear dye (1:5000) for nuclei staining. After three washes with DPBS 1x, cells were mounted onto slides using Fluoroshield mounting medium and confocal images of the fluorescently labeled proteins were captured using the Zeiss LSM900 inverted confocal microscope. For the RFP-EGFP-LC3 neuronal and astrocytic cultures were fixed immediately after the pharmacological treatments to impair autophagy with 4% formalin solution in DPBS 1x for 15min, rinsed three times with DPBS 1x and incubated in DPBS 1x together with Hoechst 33342 nuclear dye (1:5000) for nuclei staining. Then the cells were rinsed with DPBS 1x to wash out the excess of Hoechst 33342 and mounted for confocal analysis of the endogenous fluorescence.

Microglial cells were firstly washed with PBS 1x and fixed with 4% PFA for 20min at RT. Then they were permeabilized in 0.25% Triton X-100 in PBS 1x for 15min at RT and blocking was performed with 2% BSA in permeabilization buffer for 1h at RT. Primary antibodies in blocking buffer (Fkbp8 1:250, Rtn3 1:500, K63 Ubiquitin 1:1000, p62 1:1000 and P2Y12R 1:200) were incubated overnight at 4°C. After three washes with PBS 1x, samples were incubated with fluorescently labelled secondary antibodies, diluted 1:1000 in blocking buffer, for 1h at RT. After further PBS 1x washes, nuclei were stained for 5min at RT with DAPI (1µg/ml in PBS). Mowiol (polyvinyl alcohol) 4–88 was used as mounting medium.

### Confocal imaging

Imaging of the fluorescently-labelled proteins of primary cell cultures (neurons, astrocytes, oligodendrocytes, microglia) was performed using 405, 488, 594, 647nm excitation wavelengths, where confocal images (1024x1024) were acquired as z-stack (z step 0.5) for a total of 5–20µm, and through a 63x objective on the Zeiss LSM900 inverted confocal microscope (for neurons, astrocytes, oligodendrocytes) or Stellaris 5 confocal microscope (Leica Microsystems) (for microglia).

### Analysis of confocal imaging

All confocal images were processed and quantified using FIJI ImageJ. Briefly, images were max-projected and the profile of each cell was drawn using MAP2, GFAP, O4 or P2Y12R signal, and then saved as a ROI. Fixed thresholds for signal intensity were applied across experiments per cell population case, and mean intensity was measured normalized to area per cell, or per axon length when indicated. Particles number was also calculated using the function “analyze particles” of ImageJ, and was normalized to cell somatic area.

For the analysis of the confocal images of primary neurons or astrocytes, isolated from the tf-LC3 brains, the measurement of “yellow” puncta (AVs) on individual cells was performed as follows: the cell area was first recorded using the MAP2 or GFAP staining, then the brightness, contrast and threshold were adjusted for both RFP and GFP channel images and a binary image of particles present in both RFP and GFP channels was prepared. Using the “analyze particles” function of ImageJ, the number of both RFP- and GFP-positive puncta was calculated and the acquired values were normalized to the total area of each cell.

### Bioinformatic analysis

For the gene ontology (GO) analyses Shiny v0.76 online free tool was used (<http://bioinformatics.sdstate.edu/go/>). For the analysis of synaptic proteins we use the SYNGO database (<https://www.syngoportal.org/>). For the analysis of ER/Golgi proteins the human protein atlas was used (<https://www.proteinatlas.org/>). For the analysis of mitochondrial proteins the MitoCarta3.0 was used For the LIR motif analysis of the synaptic proteins the iLIR Autophagy database was used (<https://ilir.warwick.ac.uk/>).

## QUANTIFICATION AND STATISTICAL ANALYSIS

For the statistical analyses of western blot, electron microscopy and confocal microscopy experiments,  $N \geq 3$  independent experiments were conducted. The graph bars represent mean values  $\pm$  SEM. No data were excluded from analyses. Statistical analysis and graph design were performed using GraphPad Software 8.4.3. Details on statistical tests used and statistical significance are included in the figure legends.